Identifying OH Imposters in the ALFALFA Neutral Hydrogen Survey

by

Katherine Anne Suess

A senior honors thesis submitted in partial fulfillment

for the Honors Physics Bachelor of Arts Degree

at the University of Colorado

March 2015

Committee Members:

Advisor: Professor Jeremy Darling, Department of Astrophysical and Planetary Sciences

Professor John Cumalat, Department of Physics

Professor Jason Glenn, Department of Physics

Abstract

OH megamasers (OHMs) are rare, luminous molecular masers that are typically observed in (ultra) luminous infrared galaxies ([U]LIRGs) and serve as markers of major galaxy mergers. In blind emission line surveys such as the Arecibo Legacy Fast Arecibo L-Band Feed Array (ALFALFA) survey for neutral hydrogen (HI) in the local universe, OHMs at z$\sim$0.2 can mimic z$\sim$0.05 HI lines. We present the results of optical spectroscopy of ambiguous HI detections in the ALFALFA 40% data release [19] detected by WISE but with uncertain optical counterparts. The optical redshifts, obtained from observations at the Apache Point Observatory 3.5m telescope, identified 127 HI optical counterparts and discovered five new OHMs. Fifty-six candidates remain ambiguous. The new OHMs are the first detected in a blind spectral line survey.

The number of OHMs in ALFALFA matches predictions based on the OH luminosity function [14]. Additionally, the OHMs found in a blind survey do not seem to differ from those found in previous targeted surveys. This provides validation of the methods used in previous IR-selected OHM surveys and indicates there is no previously unknown OHM-producing population at z$\sim$0.2. We also provide a method for future surveys to separate OH and HI lines without expensive spectral observations. This method utilizes infrared colors and magnitudes, such as WISE (Wide Field Infrared Survey Explorer) mid-IR data. Since the fraction of OHMs found in flux-limited HI surveys is expected to increase with the redshift of the survey [7], this analysis can be applied to future flux-limited high-redshift hydrogen surveys.

Acknowledgements

I cannot begin to express my thanks to Prof. Jeremy Darling– not just for the sleepless nights of observing that made this project possible and his patience and enthusiasm guiding me through this project, but for providing me with an example of an excellent scientist and human being. Jeremy's cosmology course spurred me to try research in astrophysics, and working with him the past few years has made me unsure why I'd ever want to do something else. Not only has he taught me techniques vital to research in astrophysics, but I've learned to be critical and thorough in my work and to never stop asking questions. I hope someday I'll have a whiteboard filled with as many interesting research ideas as his.

George is owed countless thank-yous for his curiosity and immeasurable support. This project would have been so much more difficult without our countless late-night conversations and George's love of learning about any new subject from astrophysics units to maser physics and beyond.

I also want to thank everyone who made my undergraduate experiences so rewarding. Marty, Rodney, and Janet helped me complete my first successful research project and taught me how to write a scientific paper. Many of my physics and math professors made the subject material rewarding enough to make the homework assignments worth struggling through– and of course, that leads me to thank the study group. How would any of us have ever managed to graduate on our own? Eric and Joe are owed special thanks– Eric for putting up with me the most, and Joe for answering all my just-before-the-exam questions and teaching me GRE-level thermo.

Lastly, I want to thank my committee members Profs. John Cumalat, Jason Glenn, and Jeremy Darling for taking the time to read this honors thesis.

Contents

List of Tables

List of Figures

Chapter 1

Introduction and Background

In this work we identify OH megamasers (OHMs) that appear in the ALFALFA survey for neutral hydrogen (HI), confirm their properties match empirical predictions, and develop a method for separating HI and OH lines without optical spectroscopy. OHMs are rare, luminous molecular masers typically observed in ultra luminous infrared galaxies (ULIRGs) at 1667 MHz. The ALFALFA HI survey identifies local ($z \sim 0.05$) HI-emitting galaxies. From the definition of redshift, $1 + z = f_{emit}/f_{obs}$, we see that the observed frequencies for two objects with different emission frequencies can match if the objects are at different cosmological redshifts. For the observed 1420 MHz HI line at $z \sim 0.05$ to match the 1667 MHz OH line, the OHM must be at a redshift of $z \sim 0.2$.

We present the results of optical spectroscopy of 188 candidate OHMs in the ALFALFA $\alpha.40$ data release (Haynes et. al [19]). Candidate OHMs were HI lines detected by the Wide Field Infrared Survey Explorer (WISE; Wright et. al 2010 [29]), a mid-IR data source, that did not have clear optical counterparts. Candidate OHMs were observed by Prof. Jeremy Darling over a three-year program on the Apache Point Observatory 3.5 m telescope's Dual Imaging Spectrograph; the optical redshifts confirmed 127 HI sources with uncertain optical counterparts and discovered five new OHMs. One previously known OHM was additionally confirmed in ALFALFA. Using the sample of 6 ALFALFA OHMs

and over 12,000 HI matches in the ALFALFA $\alpha.40$ catalog, we endeavored to answer three main questions:

1. **Did ALFALFA find everything it should have?** The OH luminosity function (OHLF; Darling & Giovanelli 2002b [14]) describes the logarithmic luminosity distribution of OHMs in a given volume and luminosity interval, and integrating this function yields the number of expected OHMs in ALFALFA. We also check that ALFALFA found all previously discovered OHMs within the survey limits.

2. **Do the ALFALFA OHMs have the same infrared properties as previously discovered OHMs?** Previous OHM surveys (such as Baan et. al 1998 [5], Darling & Giovanelli 2000 [11], 2001 [12], 2002a [13]) used infrared selection criteria to identify potential OHMs. However, any OHMs with IR properties outside of these survey selection criteria would not be found in these targeted surveys. The ALFALFA OHMs were found in a blind survey, allowing us to test the assumptions made in previous OHM surveys.

3. **Is there a way to separate OH and HI lines without optical spectroscopy?** Several planned high-redshift HI surveys (including ASKAP-WALLABY (Duffy et al. 2012 [16]), MeerKAT-LADUMA (Holwerda et al. 2011 [20]), and ultimately the Square Kilometer Array) expect to observe HI up to redshifts of z = 1. However, the percentage of OHMs in an HI survey is expected to climb with redshift and reach 50% by z $\sim$ 1 (Baan et. al 1998 [5]). It is highly desirable to find a technique to separate HI and OH lines not only to increase the sample of known OHMs but also to greatly improve the accuracy of future HI survey catalogs.

In this work we make use of several data sources. The ALFALFA 40% data release (Haynes et. al 2011 [19]) is the basis of this work; all objects appear in the survey catalog and the recessional velocity listed in the catalog is what allows us to confirm OHMs. We make extensive use of WISE, a satellite that provides Vega magnitudes at 3.4, 4.6, 12, and

22 μm (Wright et al. 2010 [29]). We also use three colors, differences between magnitudes in adjacent WISE bands. While at first glance color does not appear to be linearly independent from magnitude, the magnitude of an object depends on its distance. Subtracting two magnitudes removes this distance dependence and proves a useful tool to compare objects at different redshifts. We also use the flux at 60 and 100 μm as measured by the Infrared Astronomical Satellite (IRAS; Saunders et. al 2000 [25]) to compute the far infrared luminosity.

1.1 OH Megamasers

While there are few known OHMs, these luminous objects can advance knowledge of distant galaxy mergers. All known OH megamasers are found in (U)LIRGs, bright starburst galaxies that are almost exclusively the products of major galaxy mergers (Clements et. al 1996 [10]). Merger phase is correlated with the far infrared (FIR) luminosity of ULIRGs, and the OHM fraction in ULIRGs is a strong function of the FIR luminosity; (Baan et. al 1998 [5]) this suggests that the presence of an OHM in a ULIRG indicates the phase of the merger. OHMs are also associated with high dense molecular gas fractions (Darling 2007 [15]), further indicating their relation to merger phase. Because OHMs are detectible to large distances, they could provide a useful tracer of the galaxy merger rate as a function of redshift. Zeeman splitting of the OH line has also been observed in several OHMs (Robishaw et. al 2008 [24]), allowing for direct measurement of magnetic fields in star-forming regions. A robust sample of OHMs could thus be used to constrain galaxy formation and merger models.

1.1.1 History and Previous OHM Surveys

The first OH megamaser was discovered by Baan et al. in 1982 [3] in Arp 220, the closest ULIRG to the Milky Way. The luminosity of the galaxy's 1667 MHz emission line

exceeded 10^3 $L_\odot$, orders of magnitude more luminous than known galactic OH masers– this led to the rise of the term 'megamaser,' used to described masers with $10^{1-4}L_\odot$. Early OHM surveys (such as Baan et. al 1985 [4]) focused on galaxies with bright radio continuum and found < 20 OHMs. The launch of IRAS allowed OHM candidates to be identified based on their infrared properties. Surveys such as Staveley-Smith et. al 1992 [26] and Norris et. al 1988 [23] used IRAS to select candidates with flat spectral indices in the far infrared and steep spectral indices in the mid-infrared, or ULIRG-like objects. Around 50 OHMs were detected before upgrades to the Arecibo telescope allowed Darling & Giovanelli (2000 [11], 2001 [12], 2002a [13]) to carry out a deep OHM survey that roughly doubled the number of known OHMs. There are ∼120 known OHMs up to $z = 0.264$, most of which are listed in Darling & Giovanelli 2002a [13].

1.1.2 Physics of Astrophysical Masers

The basic physics of astrophysical masers is very similar to laboratory lasers, except astrophysical masers do not have an optical cavity. The essential steps are familiar from undergraduate physics:

1. The gain medium– the collection of atoms or molecules that will produce the mased light– is pumped into an excited quantum state by an external energy source. Masing requires a population inversion, where more atoms or molecules are in the excited state than the ground state.

2. One of the excited molecules spontaneously decays or incoming radiation at the right frequency stimulates an excited molecule to decay. This releases a photon at same frequency as the quantum transition the molecule underwent.

3. The emitted photon encounters another excited molecule and stimulates it to emit a photon at the same frequency. These photons strike other excited molecules and produce a cascade of stimulated emission. Over a long path length (achieved in lab-

oratory lasers by an optical cavity and in astrophysical masers by simply having a large volume of gas) the photons are amplified to produce a maser.

The main difference between astrophysical masers and laboratory lasers is the lack of an optical cavity. For an astrophysical maser to form, there must be a long velocity-coherent pathway through the gain medium. Velocity coherence is required so the molecules of the gain medium are at the same Doppler shift; this ensures their atomic transitions are at the same energies and an emitted photon from one molecule will have the correct frequency to stimulate emission from another. Again because of the lack of an optical cavity, astrophysical masers are much broader than laboratory lasers. Multiple photon cascades can be produced through the gain medium along parallel velocity-coherent pathways. If those pathways are at slightly different velocities, Doppler shifting of the gas will result in slightly different masing frequencies. OH masing lines are typically $\sim$150 km s^{-1} wide.

Because astrophysical masers do not have an optical cavity, they also lack phase coherence. The optical cavity in a laboratory maser produces standing waves and allows only in-phase photons through the amplification process– without this resonance, a laser would not be coherent. Since an optical cavity is required to reproduce the long path lengths required for lasing, phase coherence and laser amplification are often conflated. The incoherence of astrophysical masers can be thought of through the branching path of an individual photon cascade or through the large number of masing spots in the maser. One photon produces two, then four, etc.; however, there is no reason that these branchings occur at the same time and thus no reason to assume coherence. Alternatively, one can consider the multiple photon cascades that produce an observed maser. There is no reason to assume that the original photons of each cascade were in phase, and thus no reason to think the observed amplified light should be coherent.

Four energy states contribute to masing in the OH molecule. J, the total angular momentum quantum number, is split in two by Λ doubling, or the interaction between the electron angular momentum and the molecular rotation. Hyperfine coupling with the nu-

clear spin (Townes & Schawlow 1975 [27]) then splits the two states again. The 1667 MHz line corresponds to the quantum transition where the the total angular momentum quantum number (including nuclear spin) remains constant, but the alignment of the electron angular momentum and the molecular rotation changes. Pumping at 35 or 53 μm can excite ground state OH to an unstable state, where it then decays to the masing state (Burdyuzha & Vikulov 1990 [8]). This pumping can be achieved though the intense FIR radiation produced in the nucleus of the ULIRG (Lockett & Elitzur 2008 [21]), while radio emission from the host galaxy's central AGN can stimulate the 18-cm emission (Baan & Klockner 2005 [6]).

The OH molecule is fairly common astophysically, though masing conditions are typically only met during galaxy merger conditions. In star-forming regions, gas experiences turbulent mixing. Because of this mixing, there is a large spread in velocities throughout the gas. However, the wide gas velocity distribution means that a spontaneously emitted photon is very likely to encounter another molecule at the same Doppler shift and cause stimulated emission. OH molecules at a different velocity and Doppler shift do not interfere with the stimulated emission cascade. Therefore, almost any path of sufficient length through the gain medium can be a velocity-coherent pathway for multiple Doppler shifts of masing. OH masers are not isotropic; instead, there are multiple 'maser spots,' individual masing beams typically too small to be resolved, that contribute to the total observed maser luminosity; (Lonsdale 2002 [22]) each spot corresponds to a different pathway through the gain medium, and can be at a different velocity and phase depending on the relative Doppler shift of the gas.

1.2 21cm Neutral Hydrogen Surveys

The 21 cm hydrogen line was first detected in 1951, and it has been a mainstay of radio astronomy ever since. Because $\sim$75% of the universe is hydrogen, the 21 cm line can be

seen in both our own Milky Way and other galaxies. Rotation curves and masses of galaxies can be calculated using the 21 cm line, and it can even be used to study the evolution of galaxies and probe fundamental physics such as the time evolution of the fine structure constant. Unsurprisingly, surveys for neutral hydrogen are an important tool in radio astronomy.

1.2.1 Physics of the 21cm Hydrogen Line

Quantum mechanics allows for exact calculation of hydrogen's energy structure. The main energy levels can be calculated to rely on the quantum number n, with energy separations given by $\frac{2\pi^2 me^4}{h^2}[\frac{1}{{n_1}^2} - \frac{1}{{n_2}^2}]$. The total angular momentum quantum number l and electron spin quantum number s also affect the energy, but split the main levels only slightly. A factor of α^2 ($\sim 5 \times 10^{-5}$) smaller than the main energy levels of the atom is the fine structure of hydrogen, which includes terms accounting for physics such as the relativistic nature of the electron and spin-orbit coupling. Even smaller is the hyperfine splitting of hydrogen's ground state, which is a result of the interaction of the electronic spin and nuclear spin– the two spins must be either parallel or antiparallel, and the energy split between the two states is a factor of m_e/m_p ($\sim 5.4 \times 10^{-4}$) smaller than the fine structure energy difference.

The hyperfine splitting is a forbidden transition, so it has a long lifetime (2.87×10^{-15} sec^{-1}) and resulting small natural width. The average mass of HI in a galaxy (from the ALFALFA catalog) is on the order of 10^9 $M_\odot$, which corresponds to $\sim10^{66}$ hydrogen atoms in a galaxy and $\sim10^{51}$ hydrogen transitions per second from an average galaxy. So despite the small likelihood of any single atom undergoing the hyperfine transition, the night sky is incredibly bright at 1420 MHz due to the incredible numbers of hydrogen atoms in a galaxy. HI surveys look at a range of frequencies to allow for Doppler shifting of the object; a local survey will look for a large peak in an object's spectrum near 1420 MHz. The frequency of the line gives the object's velocity, redshift, and distance; the integrated line emission indi-

cates the mass of hydrogen contained within the emitting galaxy; the line width indicates the galaxy's rotation speed; and if both the line width and size of the HI-emitting region is known the mass of dark matter in the galaxy can also be calculated. HI surveys have so far revealed a wealth of information about nearby galaxies, ($z < 0.1$) and higher-redshift surveys are planned to yield HI observations up to $z = 1$.

1.2.2 The ALFALFA Survey for HI[1]

The Arecibo Legacy Fast Arecibo L-Band Feed Array survey, ALFALFA, is an HI survey at the Arecibo Observatory that covers 7074 deg^2 of the sky and is expected to find 20,000 HI sources at frequencies from 1335 to 1435 MHz. The survey's detection limit is 7.7 mJy and the beam radius is about one arcminute. The Arecibo L-Band Feed Array (ALFA) used to conduct the survey consists of seven feeds, six arranged in a regular hexagon and and one at the center of the hexagon. The array is tilted at a 19° angle so that drift scan tracks sweep out different areas of the sky and the tracks are equally spaced in declination. ALFALFA is conducted in 'fixed azimuth drift mode:' the telescope pointing is fixed (except for small zenith angle adjustments to keep the tracks parallel in J2000 declination) and the sky drifts past. The survey observes each patch of sky twice, both to increase resolution and to better filter out radio frequency interference (RFI). After calibration, each drift can be viewed in position-velocity space. An observer flags regions with suspected RFI, then an automated signal extraction algorithm searches for HI detections. Multiple templates for HI lines are used to account for varying line shape and peak. A second pass over the same part of the sky allows for re-calibration and re-extraction of signals. Confirming the candidates relies on comparison of both different polarization samples and spatially adjacent samples. Data reduction and candidate confirmation is non-trivial. In this work, we use the $\alpha.40$ ALFALFA catalog (Haynes et. al 2010 [19])– this is the most recent release of ALFALFA, and contains 40% of the final survey volume.

[1]This section draws heavily on the ALFALFA design and strategy description, Giovanelli et. al 2005 [18]

ALFALFA assumes that any detectable peak in a spectrum between 1335 and 1435 MHz is neutral hydrogen. This is for the most part a very good assumption– HI is by far the dominant line in this part of the radio spectrum. Beyond HI at 1420 MHz and four OH lines at 1612, 1665, 1667, and 1720 MHz the next astrophysically important line is CH at 3264 MHz, far enough away from HI that it is unlikely to be shifted into the ALFALFA redshift range. However, we see from the definition of redshift $1 + z = f_{emit}/f_{obs}$ that lines with different rest frequencies can be observed at the same frequency if their redshift is different. This allows for OH megamasers at $z \sim 0.2$ to mimic HI at $z \sim 0.05$ and appear in the ALFALFA catalog.

We note that ALFALFA's beam radius of 1 arcmin is large enough that identifying optical counterparts for the radio sources can be tricky. Many of the HI sources found in ALFALFA are known galaxies, or in optical light appear to be large spirals that are probable sources of the detected HI. In some cases, however, no obvious optical counterpart can be found within the ALFALFA beam uncertainty; in others, multiple possible optical counterparts are within the beam uncertainty. ALFALFA sources without clear optical counterparts are the main focus of this work.

Chapter 2

Methods and Uncertainties for HI and OHM Detections

2.1 Observations

Observations were made by Prof. Jeremy Darling at Apache Point Observatory on the Dual Imaging Spectrograph (DIS) with the standard B400/R300 grating setup and a 1.5" spectroscopic slit. With this setup, the blue side of the chip has a wave center of 4400 Å and 1.83 Å/pixel linear dispersion. The red side of the chip has a wave center of 7500 Å and 2.31 Å/pixel linear dispersion. This linear dispersion produces an uncertainty of 125 km s^{-1} on the blue side and 92 km s^{-1} on the red side; this is the main contribution to the final velocity uncertainty.

2.2 Data Reduction

Raw images from DIS were reduced and analyzed by Katherine Suess using the Image Reduction Analysis Facility (IRAF). The images were trimmed, then bias and flat field corrections were performed using bias and flat images taken during each observation session. This process did not add significant uncertainty into the final line measurements.

Wavelength calibration was then performed on the flattened images. First, the IRAF routine 'identify' was used to mark positions of optical lines on a HeNeAr arc lamp spectrum taken during the observing session. After the user identified ∼6 strong optical lines from the red side of the chip and ∼4-5 lines from the blue side of the chip, the routine automatically searched for corresponding lines in the program's HeNeAr line lists. After removing obvious misidentifications, 37-48 lines were typically identified on the red side and 14-25 on the blue side. RMS values were ∼0.1 Å on the red side and ∼0.3 Å on the blue side. 'Identify' was run on the approximate spatial pixel of the spectroscopic trace for each side of the spectrum (430-450 pixels on the red side, and 400-425 pixels on the blue side, depending on observing session).

Next, the 'reidentify' routine automatically stepped through the image and reidentified the lines found with 'identify' and adjusted the wavelength solution as needed. No more than two lines from 'identify' were allowed to be lost. 'Reidentify' typically reduced the RMS uncertainties by a small amount; RMS values were ∼0.08-0.1 Å on the red side and ∼0.2-0.3 Å on the blue side. No user input was required for the reidentify process.

After identification and reidentification of the lamp lines, the 'fitcoords' IRAF task was used to fit a function of the image coordinates to the user coordinates using the results of 'reidentify'. The user chose the order of the fitting function in both the spatial and spectral direction, and had the option to delete entire identified lamp lines or identified lamp lines at specific spectral or spatial pixel values. Typically, we viewed the lamp lines with the spectral dispersion axis along the x-axis of a plot, and the residuals on the y-axis of the plot. If an entire lamp line was far from the '0' mark in this view (for example, if a line started at +0.2 and continued to +0.5, with no negative values), it was deleted. Deletion was rare– normally only the fit function order was changed. The order of the fitting function was kept the same in spatial and spectral directions; an order of 4, 5, or 6 was chosen for the red side and order 4 for the blue side. Some drift in the solution at the corners was expected– 5-15 Å was usual. If the drift increased beyond 15-20 Å and the reason

was not evident on brief examination of the image in DS9, the order was decreased despite an increase in the subsequent RMS uncertainty. Due to the smaller number of lamp lines found on the blue side, the order had to be kept lower here such that the corner values remained plausible. Typical RMS values were ∼0.05-0.1 Å on the red side and ∼0.15-0.3 Å on the blue side.

The wavelength solution from the HeNeAr calibration image was applied to the images by using the 'transform' routine. This step added uncertainty by changing the spectral axis of the spectra. With the RMS values after running 'fitcoords' of ∼0.05-0.1 Å on the red side and ∼0.15-0.3 Å on the blue side, upper bounds for the uncertainty added in this step are 4 km s^{-1} on the red side and 21 km s^{-1} on the blue side.

Following the wavelength transformation, science images of the same target were combined using 'imcombine.' Cosmic rays can cause regions of bright pixels, but tend to be in different places in different images; using median combining removes these objects more effectively than average combining. The number of images to be combined varied both with the target in question and the date of the observing session. Early targets typically had 2-4 frames for both the red and the blue side. Later targets, more likely to be HI matches, often had only 1-2 frames. Faint targets or questionable source coordinates regardless of date were often observed for 3-6 frames. The faintest targets had total exposure times of 1-2 hours, while most targets had exposure times of 5-20 minutes. Exposure time per frame was almost always 300 seconds, though some faint targets used 600 second exposure times.

Next, night sky lines were subtracted from the combined science images using the 'background' routine. Typically, the 1100-1300 pixel range was used to fit the background for both red and blue sides to capture a sufficient number of lines. If other pixel values were used in the fit for a better RMS value, they overlapped at least 50 pixels with this range and were either 200 or 250 pixels wide. This process did not add significant uncertainty to the final line measurements; it only made the final spectral lines easier to view and iden-

tify.

The final step in the data reduction corrected the wavelength scale to account for heliocentric velocity. First, the 'rvcorrect' routine in IRAF computed the heliocentric velocity correction from the date and time the spectrum was taken as well as the location of APO and the location of the object in the sky. This heliocentric velocity correction was added to the header of the image. Then, the 'dopcor' task used the correction in the header (under the label 'VHELIO') and applied the correction to the wavelength solution of the images. The sign and magnitude of the correction factor varied with date and time, but had magnitude 0-25 km s^{-1}. This process added around 1 km s^{-1} of uncertainty in the wavelength solutions, which becomes insignificant when added in quadrature with the uncertainty from the DIS grating.

2.3 Line Measurements

After calibration, we were able to take line measurements and thus determine redshifts for the objects. The IRAF task 'splot' was used for viewing spectra. The pixel value in the spatial direction was determined by examining the 2D image with DS9. In some cases, the spectrum was tilted so a distinct pixel value was chosen for each line to maximize the signal seen. The spectrum was then summed over three pixels in the spatial direction to facilitate line detection. The red side of the spectrum usually showed Hydrogen-α at 6563 Å bracketed by two [NII] lines, with a [SII] doublet on the redward side. On the blue side, the most common lines were Hydrogen-β at 4861 Å and two [OIII] lines at 5007 and 4959 Å. Other lines in the Balmer series of hydrogen as well as the 3727 Å line of [OII] were also commonly observed on the blue side. Most objects had at least 5-7 observed optical lines, with 9 lines common. Only in a few cases were fewer than 5 lines observed.

Uncertainties in line centroids were calculated using splot. RMS noise in the image was calculated in DS9 using a circular region away from the target, poorly subtracted night

sky lines, and cosmic rays. This noise estimate was passed to splot, which then calculated uncertainties in the line centroid.

Final redshifts were calculated using an error-weighted average of the individual line measurements. For each line, we measure a redshift z_i and a centroid uncertainty σ_{z_i}. If we define weights as:

$$w_i = \frac{1}{\sigma_{z_i}^2} \tag{2.1}$$

Then we can calculate the weighted average and uncertainty on the average according to:

$$z = \frac{\sum_i z_i w_i}{\sum_i w_i}; \qquad \sigma_z = \frac{1}{\sqrt{\sum_i w_i}} \tag{2.2}$$

The typical final centroid uncertainty in z is 2×10^{-6}, which corresponds to 0.6 km s^{-1}. The maximum centroid uncertainty observed was 5.4×10^{-5}, corresponding to 16 km s^{-1}.

2.4 Overall Uncertainty

There are four factors which contribute to the final uncertainty:

1. Instrument uncertainty: 112 km s^{-1} typical, 125 km s^{-1} maximum
2. Wavelength calibration: 13 km s^{-1} typical, 21 km s^{-1} maximum
3. Heliocentric calibration: 1 km s^{-1} maximum
4. Line centroid uncertainty: 1 km s^{-1} typical, 16 km s^{-1} maximum

Instrument uncertainty is by far the dominant uncertainty source, with the heliocentric calibration and line centroid uncertainty negligible. Adding all uncertainties in quadrature, we arrive at 113 km s^{-1} typical uncertainty and 128 km s^{-1} maximum uncertainty. We will thus adopt 130 km s^{-1} as the uncertainty on all cz measurements.

Chapter 3

Results of Apache Point Observations

A total of 188 objects were identified as potential OHMs and observed by Prof. Jeremy Darling at the Apache Point Observatory (APO) over 15 sessions between December 2011 and March 2013. Eight objects were observed on two different dates; three objects were observed on three dates. Objects could require multiple observing sessions for several reasons: observing conditions such as clouds, obscuration by the dawn sky, or faulty telescope guiding could prompt a second observation. However, most objects were re-observed because they were too faint, had no clear optical lines, or had multiple possible optical counterparts.

For each observation, one of three determinations could be made from the results of the redshift measurements. The first, and most common, was that the velocity of the observed object matched the velocity listed in the ALFALFA catalog within uncertainty. In this case, the object was catalogued as an HI match, the position of the optical counterpart was confirmed using SDSS and telescope pointing images, and no further analysis was performed. It was also possible for the object's velocity to match the OH velocity, in which case it was determined to be an OHM. The OH velocity was found by redshifting

the velocity in the ALFALFA catalog from the HI frequency to the OH frequency,

$$\frac{v_{OH}}{c} = \frac{\nu_{OH}}{\nu_{HI}}\left(1 + \frac{v_{HI}}{c}\right) - 1 \tag{3.1}$$

where v_{OH} is the OH velocity and ν_{OH} is the OH rest frequency. This method discovered five new OHMs in the APO observations.

The third possible determination was an ambiguous observation. Ambiguous objects matched neither the HI nor the OH velocity. For many of these objects, optical lines were visible and yielded a velocity measurement that was not within the error bars for HI or OH. This could result from an erroneous ALFALFA detection, where some non-HI line in the object's spectrum fit a template for HI and the correct redshift range for ALFALFA to mark it as HI. This was fairly common, as many of the objects we observed were marked in the survey catalog as uncertain HI detections. Alternatively, the incorrect object could have been observed. In some cases, several possible optical counterparts exist for one radio source due to ALFALFA's large beam radius. For some ambiguous cases, the telescope could have been pointed at an object that was not the source of the HI detected in the ALFALFA survey.

Also in the 'ambiguous' category were objects for which optical lines were not observable. This often occurred when the source was too faint for clear lines to be detectable or the spectra was unusually noisy due to light contamination from nearby stars. Several of the observed objects exhibited one or two currently unidentified absorption features. These 'mystery objects' require further observations with a different facility.

3.1 HI matches

One hundred and twenty-seven HI matches were confirmed through the APO observations. Each HI match was also matched with the coordinates of the optical counterpart, which occasionally differed slightly from the ALFALFA location due to large uncertainties in

the beam width. SDSS DR9 was used in conjunction with telescope pointing images to confirm the coordinates of the HI optical counterpart. The vast majority of HI matches were observed by SDSS, and positions of the few objects that did not fall within the Sloan sky coverage were confirmed using only telescope pointing images. In Table 3.1, we list all identified HI matches with their name (6-numeral strings represent AGC name), position, measured velocity, and ALFALFA velocity.

Table 3.1: Names, positions, and velocities for confirmed HI matches. The uncertainty on measured velocities is 130 km s^{-1} for all objects.

Object Name	**Position (J2000)**	**Measured Velocity (km s^{-1})**	**ALFALFA Velocity (km s^{-1})**
332417	230636.67+141014.9	12150	11962(11)
102733	000129.97+311402.9	12660	12581(12)
100783	000347.47+312037.8	5065	5011(9)
102902	000948.85+284123.8	10688	10560(8)
107	001138.13+275652.7	7488	7437(7)
102643	002136.40+252934.7	6960	7042(15)
102644	002251.55+254720.8	7188	7018(4)
HI003023+251839	003023.94+251903.9	7424	7295(14)
100291	003212.11+312459.1	6232	6140(5)
102301	004342.84+255150.8	5167	5180(8)
101685	010034.00+270552.9	11216	11040(8)
113892	010105.97+310420.9	6677	6714(6)
748808	010908.47+141357.7	9551	9551(6)
113924	012626.02+310032.5	13646	13470(6)
114047	013326.50+285623.9	7801	7700(5)
113941	014140.48+312947.0	10975	10741(3)
114121	014636.90+144129.4	7462	7485(4)
748822	015223.94+154101.0	13036	12866(5)
113956	015327.57+305349.8	11353	11205(5)
113964	015521.58+313730.6	4634	4486(7)
123118	020149.86+292647.6	16988	16909(10)
122960	020427.02+310734.6	4907	4787(7)

Table 3.1 – continued from previous page

Object Name	Position (J2000)	Measured Velocity (km s^{-1})	ALFALFA Velocity (km s^{-1})
HI020624.2+160545	020626.38+160537.7	5308	5346(8)
748838	020948.73+153346.3	10934	10774(8)
748840	021022.38+144415.0	17764	17578(5)
122141	021133.29+141419.3	3807	3797(6)
123103	021145.34+311130.2	4740	4819(10)
121499	021228.99+291055.6	9996	9920(10)
122979	021513.97+310532.3	5007	4968(6)
123005	021646.73+291236.2	5035	5159(5)
122855	021847.22+145042.3	3996	3907(4)
122988	021954.54+295050.3	11230	11080(11)
122194	022139.74+280307.2	10783	10642(7)
120193	022255.35+251835.4	4665	4584(12)
123143	022312.05+282723.0	10321	10295(6)
122859	022451.22+161039.0	8291	8189(7)
120240	022555.82+245125.3	10890	10799(16)
121216	022558.76+271613.9	10345	10171(10)
123158	023006.36+284027.2	11120	10958(4)
122883	023141.94+241721.1	5338	5409(17)
122214	023233.63+275627.3	4777	4657(3)
123163	023246.68+283310.4	10678	10660(15)
122215	023328.52+271140.5	5471	5343(2)
120342	023347.02+301121.8	10339	10253(9)
2155	024005.69+142233.3	13893	13911(6)
122421	024131.69+263744.2	1566	1586(6)
748875	024604.91+143915.3	7580	7541(7)
122850	024639.47+150856.1	7828	7791(6)
122857	024703.63+145052.2	7761	7598(5)
120529	024853.48+281624.0	5432	5424(13)
748888	024922.00+150212.4	8824	8819(3)
749015	025301.55+143720.8	9829	9891(11)

Table 3.1 – continued from previous page

Object Name	Position (J2000)	Measured Velocity (km s^{-1})	ALFALFA Velocity (km s^{-1})
122809	025905.53+271055.4	10853	10842(5)
123065	025959.21+305915.2	5924	5971(4)
748916	030647.43+143632.6	10105	10014(7)
748918	030715.30+151746.1	5687	5659(5)
174684	073019.16+060635.2	8502	8504(4)
174697	073532.65+062646.7	9719	9755(7)
174481	073602.49+133216.8	4740	4770(8)
174491	073732.29+125218.4	13970	13973(9)
170347	074035.07+260805.7	8394	8383(13)
182739	080247.11+244616.9	12463	12379(11)
188943	080520.81+055706.5	9055	9100(7)
180967	081425.33+042032.9	10117	10275(11)
749273	081709.94+263354.7	5817	5838(7)
182496	082626.15+044837.8	8531	8525(4)
183495	082907.23+275655.1	12525	12568(21)
184464	085402.71+275730.6	8094	8006(11)
749210	113201.36+272451.0	15203	15050(7)
215140	114201.27+134155.5	4435	4259(8)
HI122922+042247	122922.68+042149.0	4999	5009(7)
221030	124835.54+090732.5	7711	7558(8)
238878	130213.75+105941.9	13636	13689(9)
230239	131928.53+143439.6	6787	6705(12)
238831	132102.21+260832.9	17192	17081(8)
749554	132537.82+244712.5	10094	10076(8)
241309	140438.16+152831.8	7904	7786(15)
240736	144934.59+111453.2	16212	16426(11)
249263	145234.13+060101.7	East: 14196	14327(6)
	145235.88+060128.6	South: 14452	
248894	145949.34+152421.5	13621	13528(6)
258105	150157.40+091117.9	8988	8895(10)

Table 3.1 – continued from previous page

Object Name	Position (J2000)	Measured Velocity (km s^{-1})	ALFALFA Velocity (km s^{-1})
258530	150834.90+265155.5	17523	17513(9)
257884	151336.77+121219.9	16638	16696(7)
727058	151956.33+253618.3	9789	9695(10)
257934	154349.20+143856.5	10440	10363(19)
258337	154556.03+043250.2	6499	6440(3)
257961	155637.53+160224.3	4617	4538(7)
268208	162934.08+040227.2	16315	16255(7)
268223	162942.52+055505.3	9912	9866(7)
748649	214534.25+135511.4	8774	8788(12)
310185	215016.38+155235.0	7597	7520(6)
310204	215252.88+153418.6	13363	13169(7)
748661	215352.61+160634.1	7840	7691(6)
321219	220954.13+263156.9	11443	11355(15)
321410	221133.68+305412.6	4934	4805(8)
321209	222121.00+275033.4	12665	12706(15)
320185	222355.67+151447.2	7398	7318(6)
321344	223531.17+251039.7	12220	12108(6)
321284	223827.82+255506.5	8761	8593(18)
748716	224105.55+154924.5	1935	1936(7)
321487	224230.81+293229.5	7475	7314(11)
320379	224833.93+243205.0	12441	12319(5)
321440	225030.57+315026.6	6418	6462(3)
321453	225720.94+315315.6	6682	6660(11)
332908	230543.37+271245.0	7457	7406(6)
333370	231422.05+311505.8	7286	7235(19)
333634	231643.21+244132.2	17193	17155(13)
333525	232017.80+290859.7	6117	5956(10)
333331	232510.19+245047.9	9766	9748(9)
333286	232551.72+253821.3	8732	8582(5)
333538	232636.90+294124.2	6837	6788(7)

Table 3.1 – continued from previous page

Object Name	Position (J2000)	Measured Velocity (km s^{-1})	ALFALFA Velocity (km s^{-1})
333392	232708.92+302418.0	4541	4521(9)
333460	232854.68+310459.4	13637	13641(14)
333398	232947.29+301524.9	8393	8269(5)
331198	233211.06+285732.4	5615	5512(5)
12658	233244.76+310649.4	9615	9502(4)
233819	233816.83+254853.2	6971	6915(26)
331305	234324.28+265457.7	8252	8189(11)
333419	234411.82+314558.0	9395	9319(10)
333566	234558.61+290955.0	9784	9694(10)
333232	234628.29+274423.4	8106	8092(3)
333205	234629.35+274131.9	16815	16873(3)
331380	235345.24+253520.0	11423	11510(19)
333220	235529.43+275902.8	9191	9015(11)
333436	235648.69+302422.7	9455	9331(4)
333239	235916.77+274521.0	14615	14586(9)

3.1.1 Notes on Individual HI Matches

AGC 123005:

This spectrum showed both emission and absorption lines. The emission lines were more prevalent, but the offset absorption lines clearly showed in the blue half of the spectrum. Absorption was especially evident in Hβ and blueward Balmer series lines, where broad emission lines were nearly divided in two by the offset absorption. The emission velocity occurred at 5035 km s^{-1}, a match for the ALFALFA HI line; the absorption lines were offset to 5770 km s^{-1}. The velocity listed in Table 3.1 is the emission velocity, which matches the ALFALFA HI velocity. An SDSS optical image of the galaxy appears in Figure 3.1– the galaxy exhibits disturbed morphology, and the absorption and emission lines may be

offset because they come from different nuclei.

Figure 3.1: Optical image of AGC 123005 from SDSS. Multiple nuclei are observable; this may explain the offset absorption and emission in the optical spectrum.

HI122922+042247:

This object was identified as a clear HI match; in SDSS it was found to be a blue compact dwarf galaxy.

AGC 238831:

The optical counterpart for this object was confirmed to be the blue extended object to the west of the central ALFALFA coordinates.

AGC 249263:

Two objects were observed within the ALFALFA beam radius. One observed galaxy was to the east of the ALFALFA target coordinates, and one to the south. Both galaxies matched the HI velocity, so the coordinates and measured velocities for both are included in Table 3.1.

AGC 321440:

Most observed objects have at least five identifying spectral lines. For this object, only Hα was identified. Despite the scarcity of observable optical lines in this spectra, we are confident of the HI confirmation. The singular line is bright, shows extension along the spatial axis of the spectrum, and it is very close to the expected HI redshift. In visible light, the

object appears to be a low surface brightness galaxy.

3.2 Ambiguous Detections

Fifty-six objects remained ambiguous after observations at APO: velocities for these objects matched neither HI nor OH velocities, or no optical lines were observed. For objects that matched neither the HI nor the OH velocity, it is possible that either ALFALFA observed a non-HI line, or that APO observations were made of an object near the target that was not the optical counterpart of the ALFALFA detection. Ambiguous detections are listed in Table 3.2.

Many objects identified as OHM candidates were not clear ALFALFA detections, as clear detections can often be matched to large spirals or other objects likely to be HI sources. In ambiguous ALFALFA detections, a spectral line from the object matches one of ALFALFA's HI templates but is small, irregularly-shaped, or does not meet signal-to-noise criteria. It is usually evident upon viewing the width and peak flux of the surveyed HI line whether or not the detection was 'real.' Some of the ambiguous detections in the APO observations resulted from observations of these spurious ALFALFA detections.

When an object had multiple possible optical counterparts, the object that was observed was chosen using data from WISE. OHMs occur in ULIRGs and are typically IR-bright, so if an object within the ALFALFA beam radius was bright in the WISE 22 μm band, that object was observed at APO. This method of determining optical counterparts combined with the large beam uncertainty in ALFALFA means that some of the ambiguous detections could be observations of objects unrelated to the survey.

Ambiguous detections also include objects with no observable optical lines. Often this lack of lines is because the source was very faint and optical lines were washed out in noise or bleed-in from nearby stars. Several spectra, however, contain a small number of as-yet unidentified absorption lines. Redshifts of these few objects remain unknown even after

repeated observations at APO, and further observations must be made at another facility to determine the identity of these mystery objects.

Table 3.2: Ambiguous Detections. 'Neither' indicates that the observed velocity matches neither HI nor OH, while 'no lines' designates objects for which no optical lines were observable and no velocity determination could be made. 'ML' indicates that the ALFALFA HI detection is a marginal line, likely not a real detections. 'UL' indicates that the ALFALFA line is uncertain, and could be HI or another line.

Object Name	**Velocity (km s^{-1})**	**HI Velocity (km s^{-1})**	**OH Velocity (km s^{-1})**	**Designation**
102820	5320	4776(3)	57729	Neither
102942	10936	11585(11)	65721	Neither
102983	-	3607(18)	56356	No Lines
113863	39842	3932(10)	56738	Neither, ML
113868	30843	1922(10)	54378	Neither, ML
114080	193966	1865(10)	54311	Neither, ML, AGN
121286	18988	13052(13)	67443	Neither, UL
122433	15836	14223(17)	68818	Neither
174555	29544	2416(14)	54958	Neither, UL
189051	29971	4515(8)	57422	Neither, UL
215230	-	-	-	No Lines
215280	-	1479(4)	53858	No Lines
219219	66771	7113(11)	60472	Neither
219220	45550	6683(7)	59967	Neither
219222	24701	6218(14)	81118	Neither, ML
248933	-	2459(5)	55008	No Lines
249181	-	16288(5)	71242	No Lines, UL
249244	-	8966(8)	62647	No Lines
257889	50026	11193(8)	65261	Neither
258004	-	10552(8)	64508	No Lines, ML
258212	40857	12576(12)	66885	Neither, ML
268065	55184	10078(8)	63952	Neither
268216	82218	1723(7)	54145	Neither
330051	-	6901(7)	60223	No Lines

Table 3.2 – continued from previous page

Object Name	Velocity (km s^{-1})	HI Velocity (km s^{-1})	OH Velocity (km s^{-1})	Designation
333335	40996	5112(22)	58123	Neither, UL
333476	50343	12076(11)	66298	Neither
727130	-	2019(6)	54492	No Lines
HI000335.7+253214	-	-1319(13)	50573	No Lines
HI002048+294651	-	6799(9)	60103	Wrong Pointing
HI002957+305739	22618	-596(9)	51423	Neither
HI005058+284800	A: 87656; B: 87233	1255(11)	53595	Neither, UL
HI005555+294810	107964	1038(17)	53341	Neither, UL
HI011145+290458	A: 28224; B: 28710	16654(26)	71672	Neither, ML
HI011200+274341	33390	14232(7)	219192	Neither, ML
HI012215+284810	4321	2161(8)	54659	Neither
HI015722.6+144843	-	7589(7)	61030	Neither
HI080838.6+053210	-	9187(14)	62906	No Lines
HI113900.7+102250	73121	5118(9)	58130	Neither, ML
HI115119.4+274818	26848	14191(9)	68780	Neither, UL
39169	-	-624	51390	No Lines
HI130227+135524	83292	13344	67786	Neither
HI134330.3+111234	181209	1150(10)	53472	Neither
HI150423.7+240930	-	1217(10)	53550	Pointing Error
HI150900	22768	16663	71682	Neither, ML
HI153948.8+275213	-	9322(10)	63065	No Lines, UL
HI154718.3+043350	-	5776(9)	58902	No Lines, UL
HI215549.4+303121	-	25(2)	52151	No Lines, UL
HI020827.4+154646	-	4701(7)	57640	No Lines
HI021034.5+253405	-	17647(10)	72837	No Lines
HI022701.3+245402	64392	14966(10)	69690	Neither, UL
HI073435.3+083430	47004	168(9)	52319	Neither, UL
145944+102905	-	-	-	No Lines
150338+121443	110830	2669(6)	55255	Neither, UL
151659+051751	15363	2227(11)	54736	Neither, ML

Table 3.2 – continued from previous page

Object Name	Velocity (km s^{-1})	HI Velocity (km s^{-1})	OH Velocity (km s^{-1})	Designation
152933	39468	13749	58420	Neither, UL
HI153050.1+123632	71904	629(8)	52861	Neither, UL

3.2.1 Notes on Ambiguous Detections

AGC 102820:

The velocity determination for this object was measured from only one line, presumed to be Hα.

333335:

Again, this velocity was determined only off of one clear line presumed to be Hα.

333476

Two possible optical counterparts were observed. One matched neither OH nor HI velocities, and the other had no clear optical lines.

HI002048+294651

Possible pointing error during observations; this object may not be the WISE bright source or the ALFALFA detection.

HI002957+305739:

The α.40 data release of the ALFALFA catalog incorrectly states that this object is an OHM [19]. While the measured velocity is much higher than the ALFALFA velocity, it does not match the OH velocity and the object's identity remains unknown.

HI015722+144843:

Bleed-in from a nearby star obscured optical lines for this object.

HI134330+111234:

Two objects were observed within beam uncertainty of the ALFALFA detection. The first had no visible optical lines, and the second (the velocity listed in Table 3.2) showed broad

line emission.

HI150423+240930:

Guiding errors during observing rendered these frames unusable; no further observations were made.

150338+121443:

Due to high redshift, this object is likely an AGN.

3.3 OH Detections

Five previously undiscovered OHMs were identified during the APO observations. Additionally, one previously discovered OHM (AGC 181310) was identified in the ALFALFA $\alpha.40$ release paper [19]. These six objects are the only known OHMs in the ALFALFA database. Giovanelli et al. (2005 [18]) predicts that the survey 'should detect several additional dozen OHMs,' far in excess of the five new OHMs actually discovered.

Object Name	**Position (J2000)**	**Measured Velocity (km s^{-1})**	**ALFALFA Velocity (km s^{-1})**	**OH Velocity (km s^{-1})**
015001+240236	015001.55+240236.0	61268	7775(16)	61249(19)
022657+282457	022657.65+282457.5	64397	10185(22)	64078(26)
181310	**082312.7+275138**	**50365**	**-1551**	**50302**
219215	111125.06+052046.0	67517	13148(5)	67556(6)
145537+062437	145537.38+062437.5	68960	13749(9)	68262(11)
257959	155537.96+143905.4	61028	7393(5)	60801(6)

Table 3.3: OHM detections in ALFALFA: one previously known OHM (bold) as well as five new OHMs discovered in the APO observations. Measured velocity uncertainty is 130 km s^{-1} for all objects.

3.3.1 Luminosity and IR Properties of Detected OHMs

Previously detected OHMs have well-characterized luminosities and infrared properties. Calculating these properties for the newly discovered OHMs allows direct comparison of the ALFALFA OHM sample and previous OHM detections. Relevant properties include the total luminosity of the OHM, the flux in various IR bands from the WISE and IRAS

satellites, and the far infrared luminosity, calculated from 60 μm and 100 μm IRAS measurements. Additionally, the difference between WISE magnitudes can be calculated to obtain infrared colors. While IR color does not appear to be linearly independent from WISE magnitudes, taking the difference of two magnitudes to obtain a color removes the hidden distance variable inherent to flux measurements. IR colors can thus be used to compare OHMs independent of distance.

Using the integrated flux from the original ALFALFA detection, we found the luminosity of the source OHM. The integrated flux is given in units of Jy km s^{-1}. To convert this to a flux, we convert 1 km s^{-1} into Hz^{-1} and multiply by the frequency of the observation. To accomplish this, we use the relation

$$d\nu = \frac{dv}{c}\ \nu \tag{3.2}$$

As we are converting the unit 1 km s^{-1}, our dv is always 1. The ALFALFA survey assumes that all lines detected are neutral hydrogen with a rest frequency of 1420.4058 MHz. As such, we use the ALFALFA integrated flux and assumed HI rest frequency to obtain a flux in erg s^{-1}. If we use the assumed HI integrated flux and the rest frequency of HI, the calculated flux is independent of the line that was actually observed. Therefore, our flux calculated from HI quantities is equally applicable to the OH line that was found by the survey.

After obtaining a flux, we calculate the luminosity of the object using the standard relation:

$$F = \frac{L}{4\pi D_L^2}\ , \tag{3.3}$$

where D_L is the luminosity distance, related to the comoving transverse distance by a factor of $(1 + z)$. Luminosity distances were computed by inputing the maser redshift into Ned Wright's Cosmology Calculator [28].

We then calculated the far infrared (FIR) luminosity according to the relation from

Fullmer & Lonsdale 1989 [17] using 60 and 100 μm fluxes from IRAS.

$$L_{FIR} = 3.96 \times 10^5 D_L^2 (2.58 f_{60} + f_{100}) \ . \tag{3.4}$$

Only three of the five new OHMs appeared in IRAS; the other two fell in regions of the sky that IRAS was not able to fully cover. Luminosities and FIR properties are in Table 3.4. In Table 3.5, we list WISE colors and magnitudes for the ALFALFA OHMs.

Object Name	**OH Luminosity** ($\log(L_{OH}/L_\odot)$)	$f_{60\mu m}$ (Jy)	$f_{100\mu m}$ (Jy)	$\mathbf{L}_{FIR}$ ($\log(L_{FIR}/L_\odot)$)
022657+282457	3.29	–	–	–
015001+240236	3.61	0.301	1.064	11.87
181310	3.33	1.171	1.430	11.97
219215	3.26	–	–	–
145537+062437	3.06	0.470	1.388	12.14
257959	3.60	0.743	1.194	12.10

Table 3.4: Luminosity and IR properties of the six ALFALFA OHMs. Column (1) is the object name, (2) is the logarithm of the luminosity of the OH line (normalized to solar luminosity), (3) is the IRAS 60 μm flux density, (4) is the IRAS 100 μm flux density, and (5) is the logarithm of the FIR luminosity (normalized to solar luminosity) derived from the two IRAS fluxes according to the prescription in Fullmer & Lonsdale [17].

Object Name	**[3.4]μm**	**[4.6]μm**	**[12]μm**	**[22]μm**	**[3.4] - [4.6]μm**	**[4.6] - [12]μm**	**[12] - [22] μm**
022657+282457	13.39	12.55	9.43	7.29	0.84	3.12	2.14
015001+240236	14.23	13.61	9.82	7.47	0.62	3.74	2.35
181310	14.20	13.22	8.33	5.02	0.98	4.89	3.31
219215	15.15	14.00	9.94	7.59	1.15	4.06	2.35
145537+062437	14.60	13.72	9.54	6.60	0.88	4.18	2.94
257959	14.91	13.54	9.39	7.09	1.37	4.15	2.30

Table 3.5: Colors and band magnitudes from WISE for each OHM in ALFALFA. All units are magnitudes; WISE calibrates magnitudes to Vega [29].

Chapter 4

ALFALFA Completeness

We now compare the number of OHMs found in ALFALFA with empirical predictions. For the survey to be 'complete' with respect to OHMs, the number of OHM detections should match predictions from the OH luminosity function [14] and ALFALFA should have detected all previously known OHMs within the survey limits. This analysis provides a test for the OH luminosity function in a blind survey, helps determine the sensitivity of a blind HI survey like ALFALFA to OHMs, and may provide guidance for future HI surveys.

4.1 Known OHMs in ALFALFA

There are ∼120 known OH megamasers, the majority of which are listed in Darling & Giovanelli 2002a [13]. Known masers within the ALFALFA sky footprint and detectability limits should have appeared in the survey, and checking that they appear in the catalog is the first step in determining the completeness of ALFALFA.

The $\alpha.40$ ALFALFA data release includes 40% of the final survey, or ∼2800 deg^2 on the sky. This sky coverage is listed in Table 4.1 (Haynes et al. 2011 [19]). OHMs must also be in the correct redshift range, $0.167 \leq z_{OH} \leq 0.244$, to be detected by ALFALFA. Only 8 previously discovered OHMs lie within the volume defined by the ALFALFA sky coverage and depth. Maser spectra from Darling & Giovanelli 2000 [11], 2001 [12], and 2002a [13]

showed that only one of the eight masers in the ALFALFA volume was above the survey's 7.7 mJy flux detection limit. This OHM, AGC 181310, was indeed detected.

Right Ascension	**Declination**
07^h30^m – 16^h30^m	04°– 16 ° 24°– 28 °
22^h – 03^h	14°– 16 ° 24°– 32 °

Table 4.1: Sky coverage of $\alpha.40$ ALFALFA data release.

ALFALFA found all previously discovered OHMs within the constraints of the survey. However, we note that it only found ∼1% of all known OHMs and only found 12.5% of the OHMs within its sky footprint. ALFALFA was designed for finding strong local HI sources, not OHMs, and the detectability threshold is too high for most known OHMs to be included in the survey. This indicates that an HI survey must have a lower flux threshold than ALFALFA if detecting new OHMs is a secondary goal.

4.2 OH Luminosity Function ALFALFA Predictions

The OH luminosity function (OHLF) describes the power-law luminosity distribution of OHMs per cubic megaparsec per logarithmic luminosity interval. From Darling & Giovanelli 2002b [14], it is:

$$\phi = (9.8^{+31.9}_{-7.5} \times 10^{-6}) L_{OH}^{-0.64\pm0.21} Mpc^{-3} dex^{-1} \tag{4.1}$$

The OHLF can be used to predict the number of OHMs in ALFALFA and other HI surveys. However, the OHLF in Eqn 4.1 was developed from the results of the Arecibo Megamaser Survey (Darling & Giovanelli 2000 [11], 2001 [12], 2002a [13]), a targeted survey. The ALFALFA results provide the first opportunity to test the OHLF with data from a blind OHM survey. If the theory and predictions disagree significantly, there could be evidence for altering the OHLF.

4.2.1 Luminosity Function for the ALFALFA Survey

We use the volume, redshift range, and detection limits of ALFALFA to calculate an OHLF specific to the survey. Using the Cosmology Calculator (Wright 2006 [28], assumed cosmology flat, $H_0 = 70$ km s^{-1} Mpc^{-1}, $\Omega_m = 0.286$, $\Omega_{vac} = 0.714$), the comoving volume within ALFALFA's redshift range is 3.17 Gpc^3. The survey covers ∼1800 deg^2 (∼6.8% of the sky) so we use 6.8% of the comoving volume, or 0.21 Gpc^3, as the total volume of ALFALFA.

Next, we determine the luminosity limits of the survey. The survey could theoretically detect any hyper-luminous OHMs within its sky footprint, so the survey does not have a hard upper luminosity cutoff. However, the luminosity function was calculated based off of data from the Arecibo Megamaser Survey (Darling & Giovanelli 2000 [11], 2001 [12], 2002a [13]), and does not include data above $10^{3.8} L_\odot$. For this analysis, we choose an upper luminosity limit of $10^4 L_\odot$. This is close enough to the bounds of the Arecibo Megamaser Survey that the OHLF should still be valid; furthermore, the number of additional OHMs predicted would not change dramatically if the limit was raised due to the OHLF's power-law luminosity drop off.

The lower luminosity limit is determined by ALFALFA's 7.7 mJy detection limit. To translate this to a luminosity, we assume detected OH lines are Gaussian with a line width of 150 km s^{-1} then find the integrated flux of the minimum detected line in Jy km s^{-1}. In general, the area under a Gaussian is $ac\sqrt{\pi}$, where a is the peak value and c is the standard deviation. We can convert our line width, the full-width half-max (FWHM) of the Gaussian, to be equal to $2\sqrt{2\ln 2}\,c$; this implies that the area is $FWHM \times \frac{a\sqrt{\pi}}{2\sqrt{2\ln 2}}$. Using a line width of 150 km s^{-1} and a peak of 7.7 mJy yields an integrated flux of 0.869 Jy km s^{-1}. Converting this to a luminosity by the method described in Section 3.3.1, the lower luminosity bound is $10^{3.2} L_\odot$.

However, this method of determining a lower limit has some drawbacks. Detectability is a matter of flux density as opposed to luminosity, and the mapping between luminosity and detectability is not absolute. A tall, narrow line could have a peak value above the

ALFALFA detection limit but lower integrated flux than our calculated limit. In this case, the OHM would appear in ALFALFA but not our calculations. Alternatively, a broad low line could have a high integrated flux but a peak below ALFALFA detectability. This OHM would not be detected by the survey, but would appear in our calculations. It is not surprising, then, that one of the newly discovered OHMs actually falls below the calculated $10^{3.2} L_{\odot}$ luminosity cutoff; this omission in our predictions is likely balanced by incompleteness at and above the cutoff. There are also reliability limitations at the low-flux limit– despite identifying OHM candidates near $10^{3.2} L_{\odot}$, many could not be confirmed due to low source brightness and remain in the 'ambiguous' category (Table 3.2).

To determine an a function for the number of OHMs in the ALFALFA survey, we simply multiply the general OHLF by the volume of the survey in Mpc^3 and the luminosity span. As calculated above, the volume is 0.21 Gpc^3 and the luminosity spans a 0.8 dex interval from $10^{3.2} L_{\odot}$ to $10^{4.0} L_{\odot}$.

$$N_{ALFALFA} = (1646 \pm 5400) L_{OH}^{-0.64 \pm 0.21} \tag{4.2}$$

The Mpc^{-3} and dex^{-1} units from the general equation have been absorbed into the changes to the prefactor.

In Figure 4.1, we plot the number of expected OHMs in ALFALFA from Equation 4.2 as well as a histogram of the observed OHM distribution. We see that the observations match the predictions fairly well, with deviations of less than two OHMs per luminosity band. Keeping in mind small-number statistics and the large uncertainty on the OHLF, the two agree well.

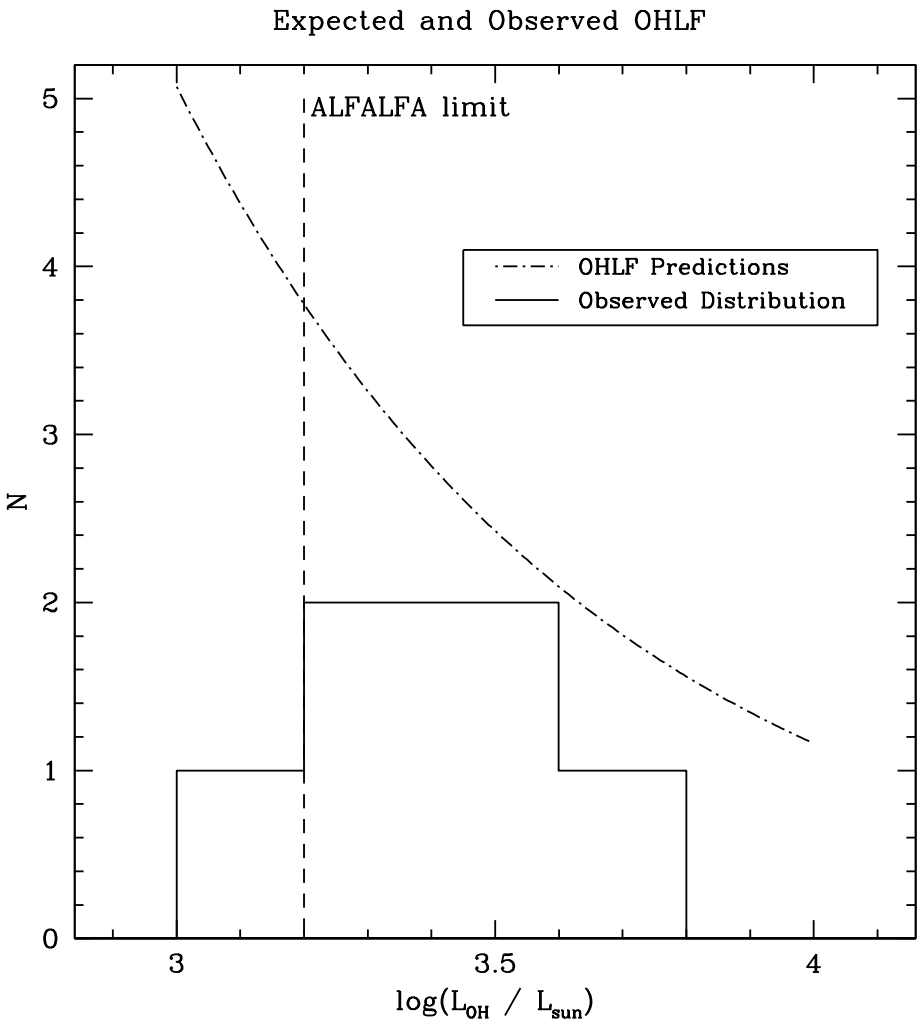

Figure 4.1: Number of OHMs as a function of luminosity. A histogram of the observed OHM distribution in ALFALFA is plotted along with predictions from the OH luminosity function. Error bars on the OHLF curve are larger than the scale of the plot, and are not plotted. We note that one OHM was found below the calculated lower cutoff on the ALFALFA survey. The ALFALFA spectrum for this object is above the flux density cutoff, but the line is narrow and has low integrated flux as we expect for objects detected below the luminosity cutoff.

4.2.2 Integrating the OHLF: Number of Expected OHMs

In general, we know that $\phi = \frac{dN}{dV d\log L}$, so $N = \int \phi \, dV d\log L$. Our original OHLF is of the form $\phi = \alpha L^{\beta}$ where $\alpha = 9.8 \times 10^{-6}$ and $\beta = -0.64$. Integrating, we obtain:

$$N = \alpha V \int_{\log L_1}^{\log L_2} 10^{\beta} d\log L \tag{4.3}$$

$$= \alpha V \int_{\log L_1}^{\log L_2} e^{\beta \log L \ln 10} d\log L \tag{4.4}$$

$$= \frac{\alpha V}{\beta \ln 10} 10^{\beta \log L} \Big|_{\log L_1}^{\log L_2} \tag{4.5}$$

Using the quantities $\alpha = 9.8 \times 10^{-6}$, $\beta = -0.64$, $\log L_1 = 3.2$, and $\log L_2 = 4.0$, we predict $N = 8.8$.

We obtain error bars by applying the upper and lower error bounds on α and β to the result of our integration. This gives uncertainty bounds of 0.03 - 137 on the number of ALFALFA OHMs. The error bars are so large due to the large quoted uncertainty in α. The total number of known OHMs in the ALFALFA survey is 6, well within error bounds of our expected 8.8. This provides further verification of the OHLF: OHMs found in a blind survey appear to follow the luminosity function calculated from the results of a targeted survey.

ALFALFA found all previously known OHMs within the survey detection limits and the total number of OHMs in the survey matches empirical predictions from the OHLF. We can therefore say that, within error, the ALFALFA survey is complete with regards to OH megamasers.

Chapter 5

Comparison of New and Existing OHMs

Previously detected OHMs were primarily found through targeted surveys (Baan et al. 1998 [5], Darling & Giovanelli 2000 [11], 2001 [12], 2002a [13], etc.). These surveys used selection criteria such as luminosity and magnitude in far-IR bands to narrow a large sample of galaxies down to a list of probable OHM hosts that were then observed. However, this work makes use of a blind HI survey to find OHM candidates and thus does not rely on assumed OHM characteristics. Comparing ALFALFA OHMs with previously discovered masers thus provides an opportunity to verify the selection criteria used in previous targeted surveys and test for a new OHM-producing environment at z$\sim$0.2.

To compare ALFALFA OHMs with previous detections, we examine the infrared properties of the two populations. The Wide-field Infrared Survey Explorer (WISE, Wright et al. 2010 [29]), provides infrared magnitudes calibrated to Vega at 3.4, 4.6, 12, and 22 μm. We also use the 60 and 100 μm flux from the Infrared Astronomical Satellite (IRAS, Saunders et al. 2000 [25]) to calculate the far infrared (FIR) luminosity according to the prescription in Fullmer & Lonsdale 1980 [17]. While all six ALFALFA OHMs appear in the WISE catalogue, only four lie within the sky footprint of IRAS. IR and FIR properties of

ALFALFA OHMs are listed in Tables 3.4 and 3.5.

We use a two-sided Kolmogorov-Smirnov (K-S) statistical test to determine if the two OHM populations come from the same distribution. The K-S test is a nonparametric statistical test that determines the probability two populations come from different distribution functions. The test is a common astrophysical tool because it works well with small sample sizes. We use a confidence level of 99%: if the K-S test result is under 0.01, the two populations show statistically significant differences. If the K-S test result is above this value, the two populations are not distinguishable. K-S test results for the IR properties of the newly discovered and previously known OHMs are listed in Table 5.1. All results are above the 1% limit, indicating that the two OHM populations come from the same IR distribution.

Infrared Property	**K-S Result**
[3.4]	0.123
[4.6]	0.326
[12]	0.175
[22]	0.103
[12] - [22]	0.038
[4.6] - [12]	0.797
[3.4] - [4.6]	0.174
60 μm flux	0.055
100 μm flux	0.015
$\log(L_{FIR}/L_{\odot})$	0.055

Table 5.1: K-S test for ALFALFA OHMs and previously discovered OHMs. All K-S results are above the 1% threshold, indicating that the two populations come from the same distribution in IR space.

We plot some infrared properties of the ALFALFA OHMs and previously discovered OHMs in Figure 5.1. The [3.4] - [4.6] color and FIR luminosity of the two populations line up well, as expected from the K-S test. While the distribution of ALFALFA OHMs in 100 μm flux vs. 60 μm flux appears biased towards the low end of the distribution, the K-S test shows this is not statistically significant. The low flux for ALFALFA OHMs is likely due to selection effects in choosing ALFALFA OHM candidates.

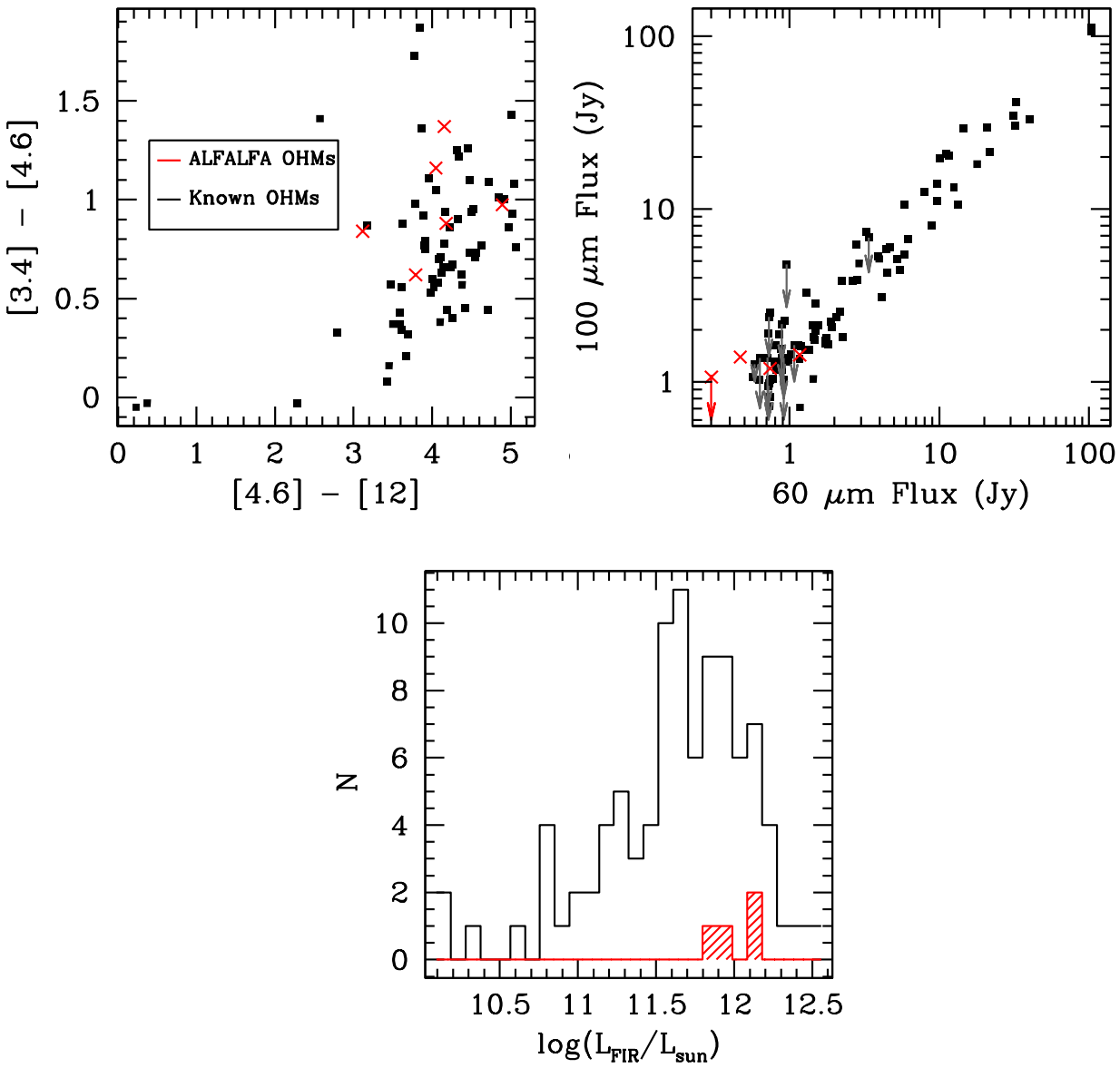

Figure 5.1: IR properties of known OHMs (in black) and ALFALFA OHMs (in red). Red and gray arrows indicate upper bounds on the 100 μm flux for ALFALFA and known OHMs. The distributions of the two populations match well, as indicated by the K-S tests in Table 5.1.

Both K-S tests and visual inspection indicate that OHMs detected in a blind survey have the same infrared properties as those detected in targeted surveys. This indicates that the IR cuts used in previous targeted OHM surveys did not exclude a significant part of the OHM population.

Chapter 6

Distinguishing OH lines from HI lines without optical spectroscopy

It is impossible to distinguish OH lines from HI lines in a survey like ALFALFA using only the survey spectra. OHMs at z∼0.2 have the same observed frequency as HI at z∼0.05 and can trigger an HI detection in the survey, and the two radio lines are nearly indistinguishable even without the variations in line shape and peak value expected when surveying 30,000 or more objects. Two example spectra from ALFALFA appear in Figure 6.1. The left object is an OHM and the right is an HI line; however, the lines look nearly identical.

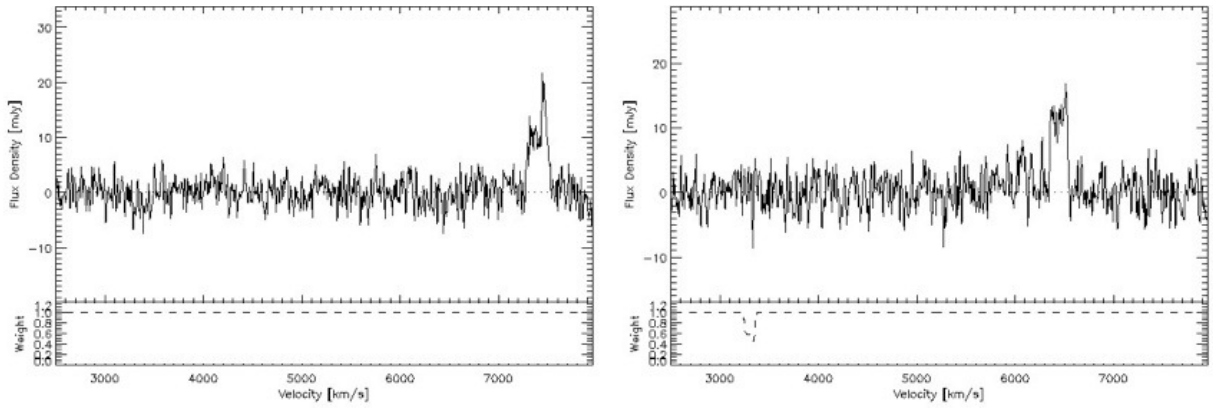

Figure 6.1: Two example ALFALFA spectra showing flux density as a function of velocity. Left is an OH line, and right is an HI line.

Given that it is difficult to distinguish between HI and OH, how important is it for an HI survey to separate populations of the two radio lines? Out of 12,416 objects in the $\alpha.40$ catalog detected by WISE, only 6 were OHMs. This is only $\sim$0.05% of the sample, a small contaminant in a large survey. However, this is mostly due to the low redshift range ($z < 0.06$) of ALFALFA: the percentage of OH lines detected in an HI survey is expected to increase with redshift both because there are more OHMs to detect at higher redshift and because isotropic HI emission is much harder to detect at large distances. Once an HI survey reaches a redshift of z = 1, it is expected to be 50% OH lines (Briggs 1998 [7]). Several high-redshift HI surveys (including ASKAP-WALLABY (Duffy et al. 2012 [16]), MeerKAT-LADUMA (Holwerda et al. 2011 [20]), and ultimately the Square Kilometer Array) are currently planned and in development. WALLABY will survey $z < 0.26$, while LADUMA and SKA aim to cover redshifts up to z$\sim$1; all of these planned HI surveys will observe a much larger population of OHMs than a low-redshift survey like ALFALFA. Not only will locating OH lines in these surveys provide a larger and more robust sample of OHMs to further science goals such as tracking the galaxy merger rate as a function of redshift, it will also improve the accuracy of the survey catalogs. While OH lines in ALFALFA are not very numerous, they are an excellent testbed for distinguishing OH lines from HI lines without the use of expensive and time-consuming optical spectroscopy.

6.1 Determining Infrared Cuts

We know that the ALFALFA OHMs exhibit similar infrared characteristics as previously discovered OHMs and that OHMs are almost exclusively found in dusty, infrared-bright galaxies. HI lines, however, are not exclusively found in IR-bright galaxies and may show different IR properties than OHMs. We performed a K-S test for the WISE colors and magnitudes, but this time compared the 6 ALFALFA OHMs with the 12,416 ALFALFA HI matches detected by WISE. Only 5,722 HI lines were detected in WISE 22 μm, so only

these objects are used for the [22] and [12] - [22] μm K-S tests. Results of the K-S tests are tabulated in Table 6.1. The test indicates that HI and OH lines are significantly different in [22], [4.6] - [12], and [3.4] - [4.6] μm.

Infrared Property	**K-S Result**
[3.4]	0.072
[4.6]	0.381
[12]	0.018
[22]	**0.003**
[12] - [22]	0.097
[4.6] - [12]	**0.010**
[3.4] - [4.6]	$\mathbf{7.32 \times 10^{-6}}$

Table 6.1: K-S test for ALFALFA OHMs and ALFALFA HI lines. K-S results for [22], [4.6] - [12], and [3.4] - [4.6] μm are below 1%, indicating the two populations come from different distributions in these magnitudes and colors.

For a visual representation of the differences the K-S test indicates, we plot histograms of the total ALFALFA sample and the fraction of OHMs as a function of each infrared property in Figure 6.2. We plotted the fraction as opposed to the number of OHMs because of the small sample size; looking at a fraction gives finer resolution. The differences in the two populations were clearly evident in the histograms, especially for the IR properties the K-S test selected. Only objects with a WISE signal-to-noise value greater than 5 are plotted; many objects are missing from 22 and 12 - 22 μm, but most ALFALFA objects were detected at 3.4 and 4.6 μm.

Using the histograms in Figure 6.2, we made cuts in IR space to separate HI and OH lines. Cuts were chosen to include all OHMs and exclude as many HI lines as possible; typically, the cut was made $\sim 0.1 - 0.2$ below the lowest OHM magnitude or color (or above the highest OHM magnitude or color) rounded to the tenths place. Reducing the sample size was an iterative process: from the initial histograms, the separation between OH and HI lines was the greatest in [4.6] - [12] μm, so the initial cut was made in [4.6] - [12] μm color. After removing objects outside of the cut, we replotted the histograms and made a second cut in a different IR parameter. We made four cuts, listed in Table 6.2.

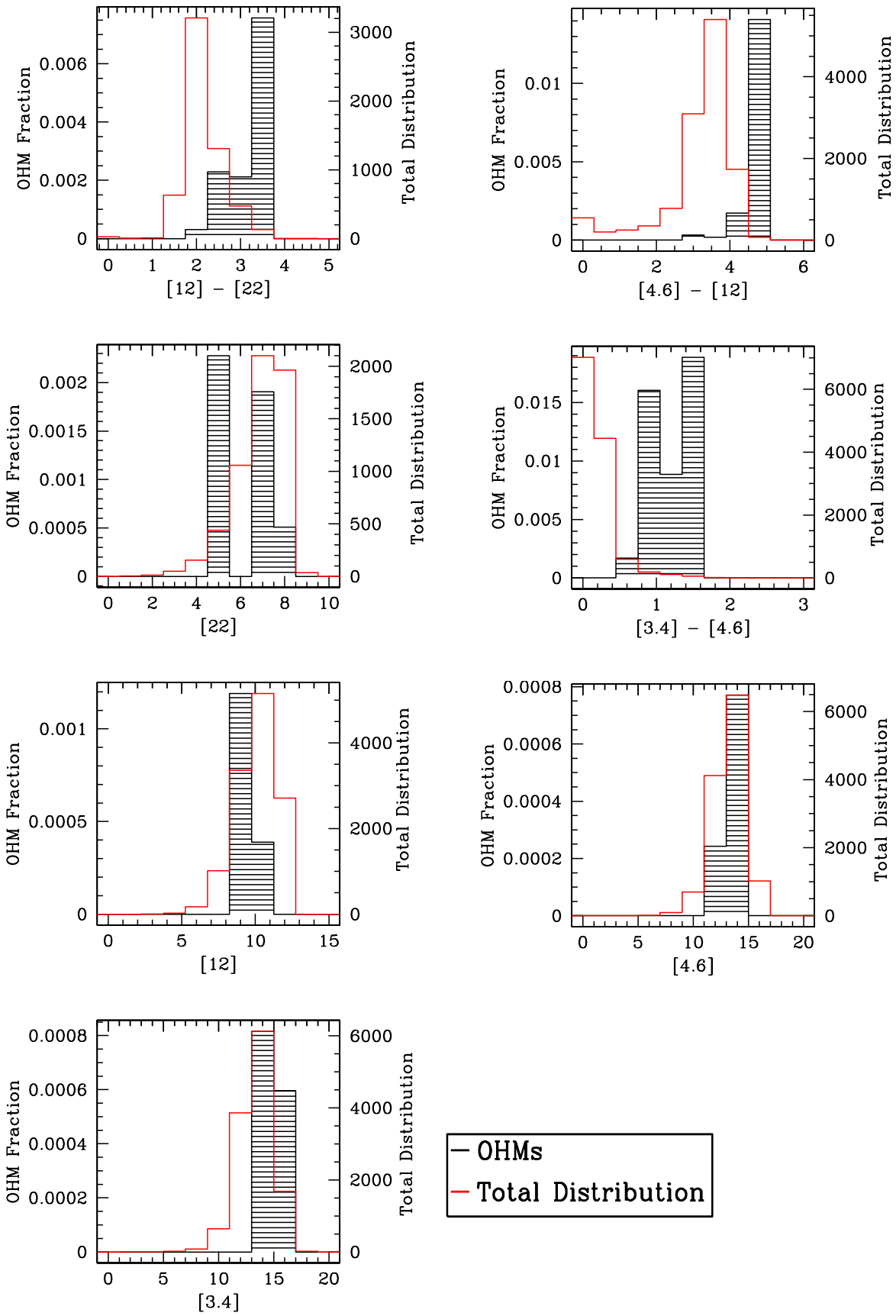

Figure 6.2: Histograms of the total distribution (red) and the OHM fraction (black). The two populations are clearly separated, especially in [4.6] - [12], [3.4] - [4.6], and [12] - [22].

Infrared Cuts
[3.4] - [4.6] > 0.6
[4.6] - [12] > 3.0
[22] > 4.8
[3.4] < 15.3

Table 6.2: Values for infrared cuts.

6.2 ALFALFA Sample After IR Cuts

After applying the infrared cuts in Table 6.2, the total sample decreased from 12,416 ALFALFA objects detected by WISE (5,722 detected at 22 μm) to 83 objects (41 detected at 22 μm). The IR cuts removed 99.3% of objects and increased the OHM fraction in the survey two orders of magnitude from 0.05% to 7.23%.

The physical mechanism underlying each infrared cut can be logically explained, indicating the locations of the cuts are not purely mathematical coincidences. The requirements for high values of [3.4] - [4.6] and [4.6] - [12] μm selects red objects and cuts out blue objects; this selects IR-bright dusty galaxies like ULIRGs that are likely to host OHMs. Due to the magnitude system's nonlinear dependence on distance, both the luminosity and the distance of the object must be considered with the magnitude cuts. OHM hosts are neither very luminous at 3.4 μm nor very close by, so they should exhibit low [3.4]. The dim [3.4] μm cut selects objects that are faint in in this band, likely removing additional nearby objects unlikely to host OHMs. OHMs are very luminous at 22 μm, but are much more distant than local HI sources. Due to the distance dependence inherent to magnitudes, this means that local HI sources could be *brighter* in [22] despite the fact that they are *less luminous* at 22 μm. The [22] μm cut is removes the brightest objects, which are likely nearby galaxies with low or moderate 22 μm luminosities unlikely to be OHM hosts. Cutting only bright [22] μm objects does not affect the large number of objects with low signal-to-noise, since objects typically show low signal-to-noise because they are not bright

enough in [22] μm for WISE to detect. Cutting bright instead of dim objects at [22] μm thus avoids issues with incompleteness.

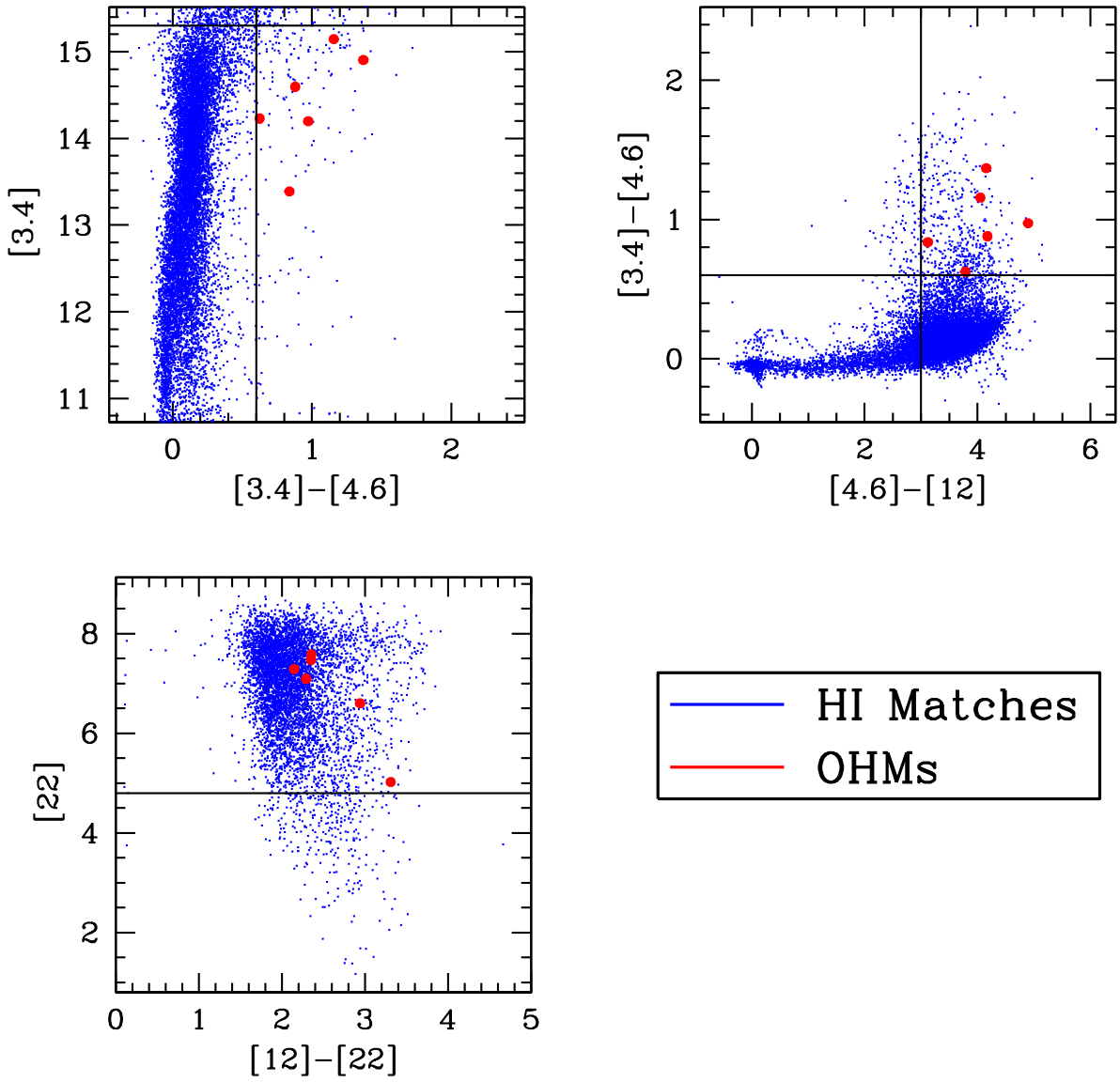

Figure 6.3: The total ALFALFA HI sample (blue) along with ALFALFA OHMs (red) in color-magnitude and color-color space. Black horizontal and vertical lines indicate the infrared cuts used to separate the sample.

The total sample of ALFALFA HI and OH lines as well as the infrared cuts from Table 6.2 are plotted in Figure 6.3. We see again the clear separation between the HI and OH populations, especially in the [3.4] vs [3.4] - [4.6] and [3.4] - [4.6] vs [4.6] - [12] plots.

While the [22] μm cut does not divide the sample to the same degree the other three cuts do, it removes $\sim$50 objects that the other cuts cannot distinguish from OHMs. We also see from Figure 6.3 that it is not necessary to modify our simple cuts into more complex cuts involving functions of more than one IR parameter– slanted lines on the plots would not cut out a large number of additional objects.

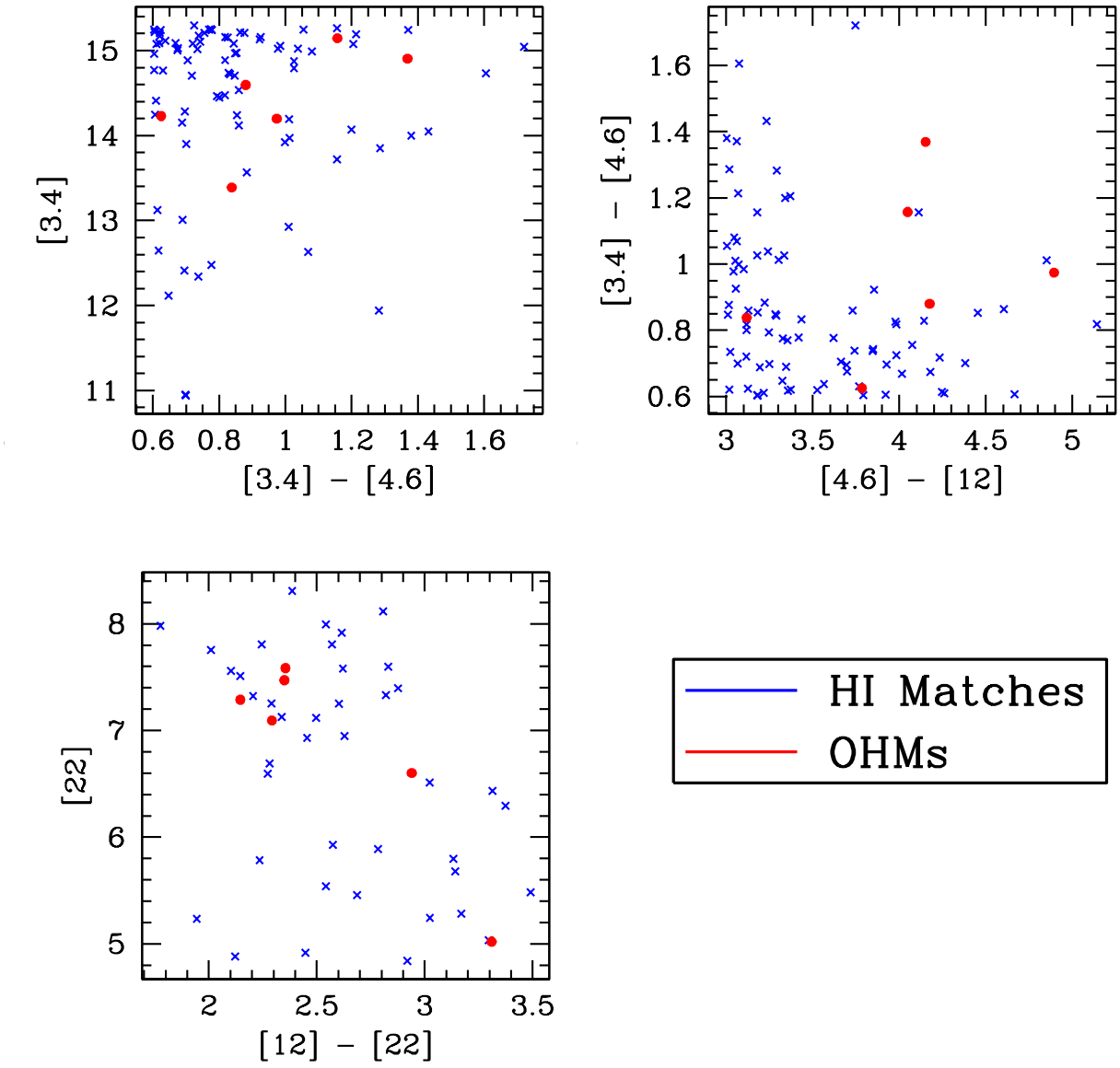

Figure 6.4: The post-cut ALFALFA HI sample (blue) along with ALFALFA OHMs (red) in color-magnitude and color-color space.

ALFALFA objects that remain after the four IR cuts are plotted in color-color and color-magnitude space in Figure 6.4. Other than a few HI outliers, the OH and HI detections that remain after the cuts are spread fairly uniformly across WISE space; this indicates that further cuts would not significantly improve the separation of the two populations.

We also re-plot the histograms in Figure 6.2 after removing all ALFALFA objects outside of the infrared cuts. These histograms, in Figure 6.5, show that the HI and OH populations now overlap in all WISE properties. While it would be possible to make an additional cut in [12] or [4.6] μm, the cut would remove less than 50 additional objects and fail to significantly increase the OHM fraction in the remaining ALFALFA sample.

A final K-S test on the post-cut samples confirms that further cuts in WISE space will not significantly improve the separation of HI and OH lines. The results (Table 6.3) show that the HI and OH populations are indistinguishable in every WISE property after the IR cuts, where before they were distinguishable or marginal in most IR properties. This indicates the effectiveness of the cuts chosen.

Infrared Property	**K-S Result Before Cuts**	**K-S Result After Cuts**
[3.4]	0.072	0.547
[4.6]	0.381	0.136
[12]	0.018	0.016
[22]	0.003	0.663
[12] - [22]	0.097	0.452
[4.6] - [12]	0.010	0.038
[3.4] - [4.6]	7.32×10^{-6}	0.258

Table 6.3: K-S test for ALFALFA OHMs and ALFALFA HI lines after IR cuts. After the cuts, the test indicates that the OH and HI populations come from the same statistical distribution.

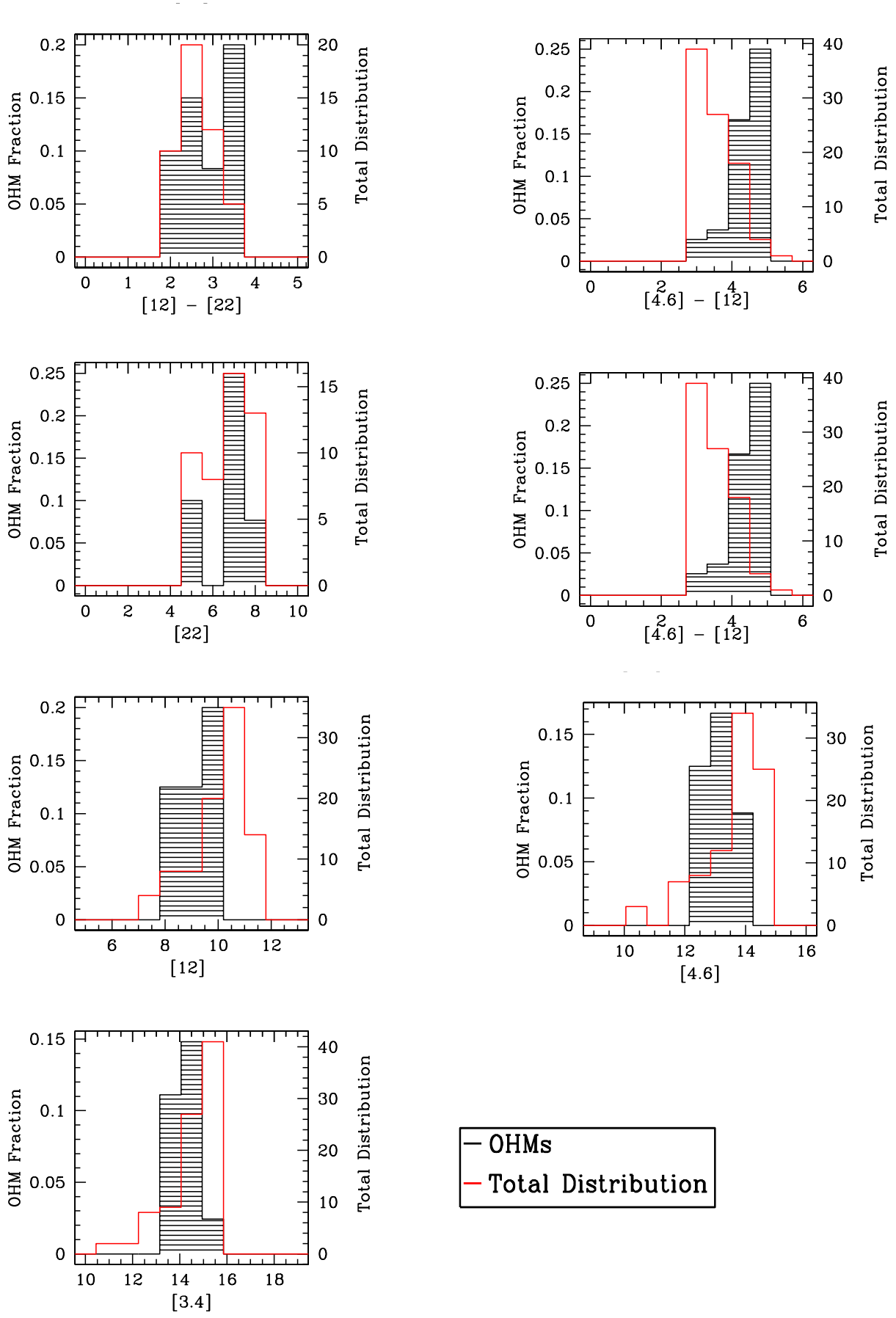

Figure 6.5: Histograms of the total distribution (red) and the OHM fraction (black) after the infrared cuts. The two populations are no longer clearly separated.

6.3 ULIRG Redshift Evolution

As redshift increases, observed wavelength will increase and the WISE bands will observe a different part of the host galaxy's spectrum. Depending on the object's spectral energy distribution (SED), it could appear brighter or dimmer as redshift increases. It is therefore necessary to introduce a redshift dependence to the magnitude and color cuts listed in Table 6.2.

In order to project WISE observations of OHMs to higher redshift we must assume an SED for the OHMs; we used Arp 220, the closest OHM, as a template. The SED was created using Spitzer spectra from Armus et. al 2004 [2] and modeled using results from Chary & Elbaz 2001 [9]. A. Truebenbach provided the results: the expected flux observed in each WISE band from redshift 0.1 to 5.0 in steps of 0.1. A simple calculation converts flux to the Vega magnitudes used in the rest of this work. For an HI survey with an upper bound of $z_{HI} \sim 1$, the OH redshift bound is $z_{OH} \sim 1.4$. In Figure 6.6, we plot the redshift evolution of Arp 220 and our infrared cuts in WISE color-color and color-magnitude space.

We see that the Arp 220 track stays within the IR cuts for the ALFALFA redshift range $z_{OH} \leq 0.25$, indicating that the cuts chosen do include OHMs in ALFALFA out to $z \sim 0.25$. The tracks then evolve out of the IR cuts, which confirms that the IR cuts must be a function of the survey redshift. The shape of the track indicates how the cuts should evolve to be applied to planned future HI surveys. Additional work must be done to find a mathematical expression for each cut's redshift evolution. We also note that the redshift evolution results in most OHMs being undetectable in the [22] μm band by a redshift of $z \sim 0.8$. Care must be taken to apply these cuts directly to future surveys at higher redshifts due to this decreasing flux; however, it may be possible to continue to separate HI and OH lines by applying the techniques used to make the WISE cuts to other data sets with lower magnitude cutoffs.

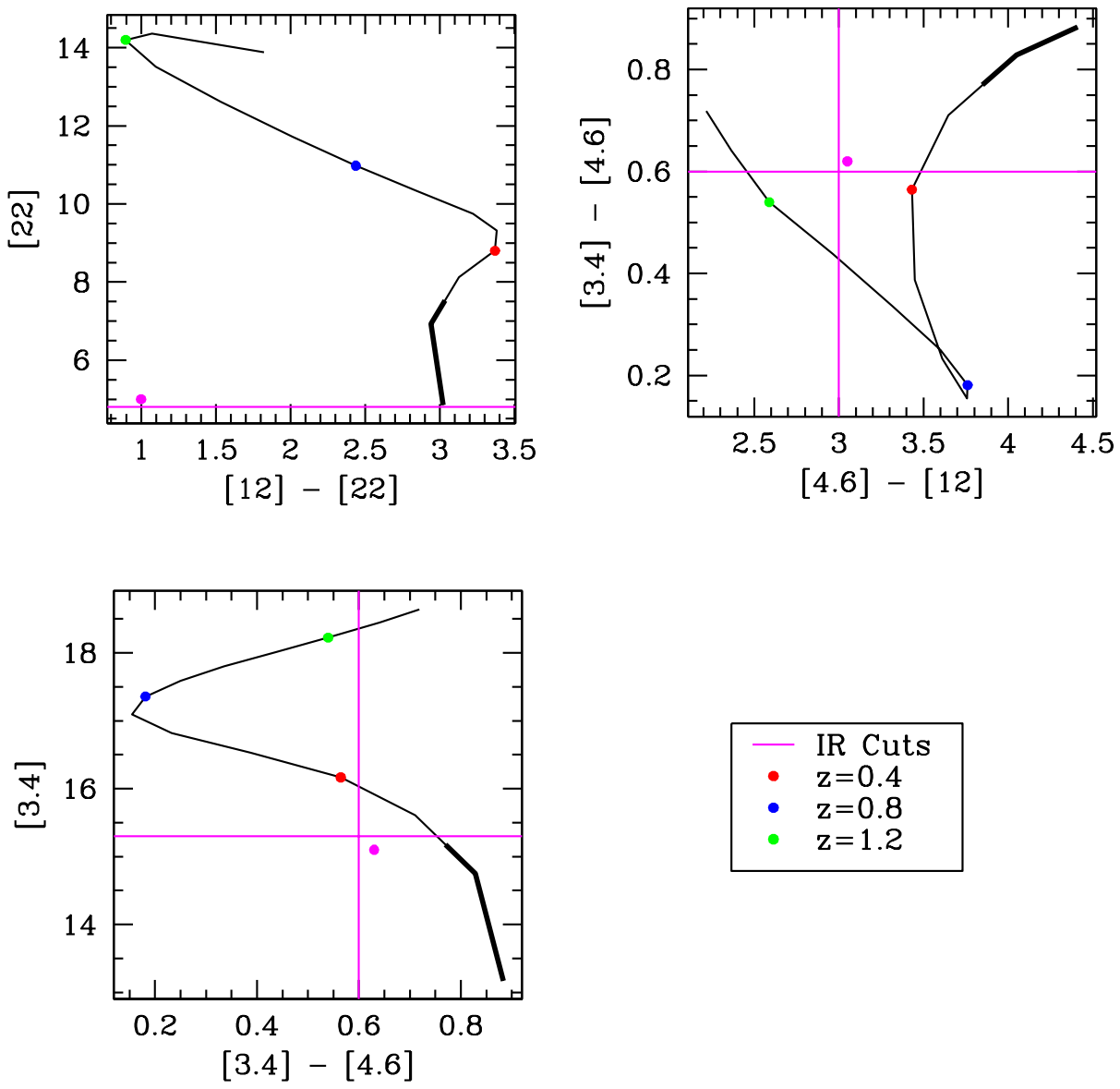

Figure 6.6: Track of the redshift evolution of Arp 220. Red, blue, and green dots mark z = 0.4, 0.8, and 1.2, while the bold portion of the track marks the ALFALFA redshift range. Magenta lines are the IR cuts, while the magenta dot represents the quadrant or half of the plot that remains after IR cuts. The tracks stay within the desired region through the ALFALFA redshift, z=0.1-0.25. Evolution past this point governs how the cuts should be adjusted for increasing redshift.

Chapter 7

Conclusions

In this work, we identified and analyzed OH megamasers in the ALFALFA survey for neutral hydrogen. 188 candidate OHMs were identified by Prof. Darling and optical spectra were taken with the Dual Imaging Spectrograph at the Apache Point Observatory. The data was reduced and line measurements were made by K. Suess; the optical redshifts confirmed 127 uncertain HI optical counterparts and discovered 5 new OH megamasers. Using the sample of all ALFALFA objects detected by WISE, the five new ALFALFA OHMs plus one previously known OHM detected by the survey, and the ∼120 previously known OHMs we were able to answer the following science questions:

1. Does the number of OHMs in ALFALFA match empirical predictions?

2. Do the OHMs found in a blind survey match the IR properties of OHMs found in previous targeted surveys?

3. Can OH lines be distinguished from HI lines using IR data from WISE?

The OH luminosity function (OHLF, Darling & Giovanelli 2002b [14]) describes the number of OHMs expected per logarithmic luminosity interval per volume. Integrating the OHLF over the sky footprint, redshift range, and luminosity detection limits of ALFALFA yields the number of OHMs expected in the survey. The function predicts AL-

FALFA should find 8.8 OHMs, well within error bounds of the 6 OHMs detected. Furthermore, only one previously known OHM lay within the survey's volume and detection limit; this OHM was detected by the survey. ALFALFA both matches predictions from the OHLF and found all previously known OHMs within survey limits, so we determine that ALFALFA is complete with respect to OHMs. However, we note that ALFALFA found less than 15% of the known OHMs within its sky footprint; this indicates that if future HI surveys wish to detect OHMs as a secondary goal they must have lower detection limits than ALFALFA.

Previous OHM surveys selected maser candidates based on their infrared properties. However, the ALFALFA OHMs were found in a blind survey. This provides us with the opportunity to compare the two OHM populations to verify the selection criteria used in previous surveys and determine if there is any previously unknown OHM-producing population at z$\sim$0.2. Kolmogorov-Smirnov statistical tests showed that the two OHM populations came from the same statistical distribution in seven WISE properties ([3.4], [4.6], [12], [22], [3.4] - [4.6], [4.6] - [12], and [12] - [22] μm), verifying the assumptions of previous OHM surveys that the masers are found in IR-bright galaxies.

Finally, we used WISE data to determine if OH lines can be distinguished from HI lines without the use of expensive optical spectroscopy. This is of particular interest for planned high-redshift HI surveys such as ASKAP-WALLABY (Duffy et. al 2012 [16]) and MeerKAT-LADUMA (Holwerda et. al 2011 [20]) as the percentage of OH lines in an HI survey is expected to increase with redshift and reach 50% by z = 1 (Briggs 1998 [7]). Kolmogorov-Smirnov statistical tests confirmed that the ALFALFA HI and OH populations came from statistically different distributions in [22], [4.6] - [12], and [3.4] - [4.6] μm. Four IR cuts, listed in Table 6.2, allowed us to remove over 99% of the HI sample and increase the OH fraction in ALFALFA two orders of magnitude from 0.05% to 7.23%. After the cuts, Kolmogorov-Smirnov tests could not distinguish the OH and HI populations and histograms of the two sets of lines overlapped, indicating that further cuts in WISE space

cannot further separate the two populations. It is possible, however, that the OHM fraction could be increased beyond 7.23% using additional data. One potential data source is the Sloan Digital Sky Survey (Ahn et. al 2014 [1]): morphology and optical properties could remove additional HI matches not distinguishable with WISE. While a separation scheme based only on WISE data can distinguish OH from HI, future work should investigate further cuts using another data source before the advent of high-redshift HI surveys.

Using data from the Apache Point observations as well as ALFALFA, WISE, and IRAS we were able to answer all three of our science questions: the number of OHMs in ALFALFA matches empirical predictions, the ALFALFA OHMs come from the same IR distribution as previous OHMs, and OH lines can be distinguished from HI lines without the use of optical spectroscopy.

Bibliography

[1] Ahn, C. P., R. Alexandroff, C. Allende Prieto et al., The Tenth Data Release of the Sloan Digital Sky Survey: First Spectroscopic Data from the SDSS-III Apache Point Observatory Galactic Evolution Experiment, *Astrophysical Journal Supplement*, **211**, 17, 2014.

[2] Armus, L., V. Charmandaris, H. W. W. Spoon, J. R. Houck, B. T. Soiffer, et al., Observations of Ultraluminous Infrared Galaxies with the Infrared Spectrograph (IRS) on the Spitzer Space Telescope, *Astrophysical Journal Supplement*, **154**, 178, 2004.

[3] Baan, W. A., P. A. D. Wood., A. D. Haschick, Broad Hydroxyl Emission in IC 4553, *The Astrophysical Journal*, **260**, L49-L52, 1982.

[4] Baan, W. A., A. D. Haschick, J. T. Schmelz. The Fourth OH Megamaser: Markarian 273, *The Astrophysical Journal Letters*, **298**, L51-L54, 1985.

[5] Baan, W. A., J. J. Salzer, & R. D. LeWinter. Optical Classification of Megamaser Galaxies, *The Astrophysical Journal*, **509**, 633-645, 1998.

[6] Baan, W. A. & H.-R. Klockner. Radio Properties of FIR-megamaser nuclei, *Astronomy & Astrophysics*, **499**, 559-568, 2006.

[7] Briggs, F. H. Cosmologically distant OH megamasers: A test of the galaxy merging rate at Z $\sim$ 2 and a contaminant of HI surveys in the 21cm line. *Astron. Astrophys*, **336**, 815-822, 1998.

[8] Burdyuzha, V. V. & K. A. Vikulov. The excitation and physical nature of megamasers, *M*onthly Notices of the Royal Astronomical Society, **244**, 86-92, 1990.

[9] Chary, R. & D. Elbaz. Interpreting the Cosmic Infrared Background: Constraints on the Evolution of the Dust-enshrouded Star Formation Rate, *The Astrophysical Journal*, **556**, 562-581, 2001.

[10] Clements, Sutherland et al. MNRAS 277, 447-497, 1996.

[11] Darling, J. & R. Giovanelli. A Search for OH Megamasers at z $>$ 0.1. I. Preliminary Results, *The Astronomical Journal*, **119**, 3003-3014, 2000.

[12] Darling, J. & R. Giovanelli. A Search for OH Megamasers at z $>$ 0.1. II. Further Results, *The Astronomical Journal*, **121**, 1278-1293, 2001.

[13] Darling, J. & R. Giovanelli. A Search for OH Megamasers at z $>$ 0.1. III. The Complete Survey, *The Astronomical Journal*, **124**, 100-126, 2002a.

[14] Darling, J. & R. Giovanelli. The OH Megamaser Luminosity Function, *The Astrophysical Journal*, **572**, 810-822, 2002b.

[15] Darling, J. A Dense Gas Trigger for OH Megamasers, *The Astophysical Journal*, **669**, L9-L12, 2007.

[16] Duffy, A. R., M. J. Meyer, L. Staveley-Smith, M. Bernyk, D. J. Croton, et al., *Monthly Notices of the Royal Astronomical Society*, **426**, 3385-3402, 2012.

[17] Fullmer, L. & C. Lonsdale. Catalogued Galaxies and Quasars Observed in the IRAS Survey (Pasadena: JPL), 1980.

[18] Giovanelli, R., M. Haynes, B. Kent, et al. The Arecibo Legacy Fast ALFA Survey: I. Science Goals, Survey Design and Strategy, *The Astronomical Journal*, **130**, 2598-2612, 2005.

[19] Haynes, M. P., R. Giovanelli, A. M. Martin, K. M. Hess, A. Saintonge, et al. The Arecibo Legacy Fast ALFA Survey: The $\alpha.40$ HI Source Catalog, Its Characteristics and the Derivation of the HI Mass Function, *The Astronomical Journal*, **142**, 142-170, 2011.

[20] Holwerda, B. W., S.-L. Blyth, A. J. Baker. Looking at the Distant Universe with the MeerKAT Array (LADUMA). *The Spectral Energy Distribution of Galaxies Proceedings IAU Symposium* **284**, 2011.

[21] Lockett, P. & M. Elitzur. The Effect of 53 μm IR Radiation on 18 cm OH Megamaser Emission. *The Astrophysical Journal*, **677**, 985,-992, 2008.

[22] Lonsdale, C. J. Cosmic Masers: From Proto-Stars to Black Holes, *IAU Symposium*, **206**, ed. V. Migenes & M. J. Reid, 413, 2002.

[23] Norris, R. P., F. F. Gardner, J. B. Whiteoak. A search for megamaser galaxies, *Monthly Notices of the Royal Astronomical Society*, **237**, 673-681, 1998.

[24] Robishaw, T., E. Quataert, C. Heiles. Extragalactic Zeeman Detections in OH Megamasers, *The Astrophysical Journal*, **680**, 981-998, 2008.

[25] Saunders, W., W. J. Sutherland, S. J. Maddox, O. Keeble, S. J. Oliver et al., The PSCz catalog, *Monthly Notices of the Royal Astronomical Society*, **317**, 55-63, 2000.

[26] Staveley-Smith, L., R. P. Norris, J. M. Chapman, D. A. Allen, J. B. Whiteoak, A. L. Roy. A southern OH megamaser survey, *Monthly Notices of the Royal Astronomical Society*, **258**, 725-737, 1992.

[27] Townes, C. H. and A. L. Schawlow. Microwave Spectroscopy, Dover Publications, New York 1975.

[28] Wright, E. L. A Cosmology Calculator for the Wold Wide Web, *Publications of the Astronomical Society of the Pacific*, **118**, 1711-1715, 2006.

[29] Wright, E. L., P. R. M. Eisenhardt, A. K. Mainzer, M. E. Ressler, R. M. Cutri, et al. The Wide-Field Infrared Survey Explorer (WISE): Mission Description and Initial On-Orbit Performance, *The Astronomical Journal*, **140**, 1868-1881, 2010.